

# SparsePixels: Efficient Convolution for Sparse Data on FPGAs

**HO FUNG TSOI**, University of Pennsylvania, USA

**DYLAN RANKIN**, University of Pennsylvania, USA

**VLADIMIR LONCAR**, Institute of Physics Belgrade, Serbia

**PHILIP HARRIS**, Massachusetts Institute of Technology, USA and Institute for Artificial Intelligence and Fundamental Interactions, USA

Inference of standard convolutional neural networks (CNNs) on FPGAs often incurs high latency and a long initiation interval due to the deep nested loops required to densely convolve every input pixel regardless of its feature value. However, input features can be spatially sparse in some image data, where semantic information may occupy only a small fraction of the pixels and most computation would be wasted on empty regions. In this work, we introduce SparsePixels, a framework that implements sparse convolution on FPGAs by selectively retaining and computing on a small subset of active pixels while ignoring the rest. We show that, for identifying neutrino interactions in naturally sparse LArTPC images with 4k pixels, a standard CNN with a compact size of 4k parameters incurs an inference latency of  $48.665\ \mu\text{s}$  on an FPGA, whereas a sparse CNN of the same base architecture, computing on less than 1% of the input pixels, achieves a  $\times 73$  speedup to  $0.665\ \mu\text{s}$  with resource utilization well within on-chip budgets, trading only a small percent-level performance loss. This work aims to benefit future algorithm development for efficient data readout in modern experiments with latency requirements of microseconds or below. Code is publicly released at <https://github.com/hftsoi/sparse-pixels>.

**CCS Concepts:** • **Hardware** → **Reconfigurable logic and FPGAs**; • **Computing methodologies** → **Computer vision; Neural networks**.

**Additional Key Words and Phrases:** Convolutional Neural Network, Sparse Data, Low-Latency Inference, FPGA

**ACM Reference Format:**

Ho Fung Tsoi, Dylan Rankin, Vladimir Loncar, and Philip Harris. 2025. SparsePixels: Efficient Convolution for Sparse Data on FPGAs. 1, 1 (December 2025), 26 pages. <https://doi.org/XXXXXX.XXXXXXX>

## 1 Introduction

Convolutional neural networks (CNNs) have gained wide interest and usage for image-based recognition tasks in particle physics experiments, including muon tracking in gas chambers [17, 27, 42], jet flavor tagging in calorimeters [12, 23, 35, 43, 46], anomaly detection for new physics searches at colliders [3, 21, 22, 28, 30, 34], and neutrino identification in liquid argon time projection chambers (LArTPCs) [4, 7, 10, 16, 24]. This is because often experimental data are encoded in geometrical formats originating from detector layouts and can be represented in fixed-grid views. Hence, it is natural to use CNNs to process and extract signal from this type of data. However, some of these images are spatially very sparse because certain signals leave small traces within large detector volumes. For example, in the dataset presented in [42], a

---

Authors' Contact Information: **Ho Fung Tsoi**, ho.fung.tsoi@cern.ch, University of Pennsylvania, USA; **Dylan Rankin**, dsrankin@sas.upenn.edu, University of Pennsylvania, USA, ; **Vladimir Loncar**, vladimir.loncar@cern.ch, Institute of Physics Belgrade, Serbia; **Philip Harris**, pharris@mit.edu, Massachusetts Institute of Technology, USA and Institute for Artificial Intelligence and Fundamental Interactions, USA.

---

Permission to make digital or hard copies of all or part of this work for personal or classroom use is granted without fee provided that copies are not made or distributed for profit or commercial advantage and that copies bear this notice and the full citation on the first page. Copyrights for components of this work owned by others than the author(s) must be honored. Abstracting with credit is permitted. To copy otherwise, or republish, to post on servers or to redistribute to lists, requires prior specific permission and/or a fee. Request permissions from [permissions@acm.org](mailto:permissions@acm.org).

© 2025 Copyright held by the owner/author(s). Publication rights licensed to ACM.

Manuscript submitted to ACM

muon traversing gas chambers leaves a track in a 2D image covering the full muon station, but a single muon track may occupy only 10 out of  $9 \times 384$  pixels ( $< 0.3\%$  of the input). Similarly, in neutrino experiments, particle tracks in large LArTPC volumes can have, on average, only 0.01% nonzero pixels [24]. Because these signatures can have irregular shapes and appear anywhere in the image, CNNs must scan the entire input to capture them. Implementing large standard CNNs can therefore incur high inference latency even on high-speed custom processors such as FPGAs [2], posing a challenge for data readout in modern experiments that enforce ultra-low latency.

In modern particle experiments, data processing is typically divided into two domains: online (low-latency) processing and offline analysis. Taking the CERN Large Hadron Collider (LHC) as an example [1, 19, 20, 47], proton bunches collide at 40 MHz, and each collision is an event. The detector acts like a high-speed camera, recording trajectories and energy deposits across subdetectors. The resulting raw information is about 1 MB per event, leading to a raw data rate of  $\mathcal{O}(10)$  TB/s. Storing all data is impossible due to limited bandwidth and storage capacity, hence a fast filtering system (the trigger) is required to select potentially interesting events for permanent storage in real time, concurrent with the 40 MHz collisions. Because the input streams in at 40 MHz, the Level-1 trigger must decide whether to store an event within a few microseconds, set by buffer capacity, motivating the use of FPGAs/ASICs for real-time processing. It is crucial and challenging to design trigger algorithms for online use that are sensitive enough to select interesting events (as unselected events are discarded permanently) while remaining compact enough to meet low-latency constraints. With the forthcoming High-Luminosity LHC upgrade [61], developing more sophisticated and hardware-efficient online algorithms is essential for handling unprecedented rates and bandwidth. After trigger selections, data are stored and analyzed offline without strict latency limits.

In this paper, we focus on the low-latency domain, targeting inference latencies on the order of microseconds and below. The general workflow for deploying machine learning (ML) models on FPGAs in this regime is well established in the community. The `hls4ml` library [25, 26] is widely used due to its flexible hardware-aware configuration, which supports translating trained models from common Python libraries into High-level Synthesis (HLS) firmware for FPGA deployment. CNNs are supported and have been benchmarked [2, 29, 52]. For large images (e.g., with  $\mathcal{O}(1000)$  or more pixels), inputs typically cannot be fully partitioned to enable parallel processing on an FPGA, so designs fall back to a streaming approach, processing one pixel at a time. While this keeps resource usage small, it often yields high latencies. When the image is sparse, say only a few percent or fewer pixels are nonzero on average, the standard convolution becomes highly inefficient because it must be computed on many empty regions. Therefore, we investigate a class of CNNs that adaptively select and compute only on active pixels, targeting large images with extreme sparsity.

### Problem statement.

- Can we improve the processing efficiency of CNNs for spatially sparse images on FPGAs to allow for accelerated real-time inference in experiments that require microsecond-level latency or below?

### Our contributions.

- (1) Development of a sparse convolution method designed for low-latency FPGA implementation.
- (2) Proof-of-concept on spatially sparse image data, demonstrating significant FPGA inference speedups with comparable model performance.
- (3) A Python library for quantization-aware training of sparse CNNs and C++ HLS modules for FPGA deployment. Code is publicly released at <https://github.com/hftsoi/sparse-pixels>.

In the rest of the paper, Sec. 2 reviews related developments that motivate this work, Sec. 3 introduces the SparsePixels framework for sparse CNN training and FPGA implementation, and Sec. 4 presents the experimental setup and validation results.

## 2 Related work

Our work aims to improve upon the current implementation of standard 2D convolution in `hls4ml` [2] designed specifically for sparse image data on FPGAs in the low-latency regime, using a sparse convolution method inspired by works on acceleration of sparse 3D point cloud inference.

**Low-latency standard convolution on FPGAs.** The `hls4ml` [25, 26] library is open-sourced and developed to facilitate deployment of ML models on FPGAs for fast inference in strictly constrained environments such as particle physics experiments at the LHC. The library provides a Python interface for translating models trained in common libraries such as Keras [14, 18] and PyTorch [44] into high-level C/C++ via HLS tools, which can be synthesized into register-transfer level (RTL) designs, enabling rapid customization and optimization of resources and latency for FPGA firmware. `hls4ml` has integrated quantization-aware training (QAT) for fixed-precision deployment [18, 49]. Implementation of various ML architectures have been demonstrated [25, 33, 36, 48, 53, 54], including CNNs [2, 29, 52], which serve as the baseline in this paper. Other tools such as FINN [11, 55] and Chisel4ml [56], with slightly different optimization targets and workflows, also support low-latency inference of standard convolution on FPGAs. However, across all these tools, the underlying challenge is similar: the amount of computation required by standard convolution on large inputs makes full parallel processing prohibitive, forcing designs toward streaming implementations (inputs are processed serially) that can incur too high a latency for real-time systems. For example, `hls4ml` has demonstrated an inference latency of 5  $\mu$ s for CNNs on  $32 \times 32$  images [2], and this latency grows rapidly with input size.

**Efficient convolution on GPUs.** A direction to reduce CNN computation is to exploit sparsity to skip unnecessary operations. [40] explored model compression via parameter pruning, reducing redundancy in the parameter space and mapping convolutions to sparse matrix multiplications for speedup. Other works [41, 60] explored efficient data-flow schemes on FPGAs for CNNs with sparse structure to skip multiplications involving zeros. These methods focus on weight sparsity or structured sparsity, and still operate on all input pixels. Moreover, directly skipping computation based on irregular input sparsity often leads to input-dependent computations and varying runtimes, which is problematic in systems with strict latency bounds. A more relevant direction is to focus on selective computation only on a subset of pixels from the input tensor and ignore the rest. [31] proposed a type of sparse convolution that computes an output pixel only when any of the input pixels within the kernel receptive field is nonzero, so the computational cost scales with the number of nonzero input pixels rather than the entire image/volume. However, this approach can rapidly increase the number of nonzero pixels across convolutional layers: an output pixel can become nonzero if its receptive field includes any neighboring nonzero input, effectively dilating the nonzero set. To address this, [32] constrains the operation so that an output pixel is computed only when the same location at the input is nonzero, keeping the sparsity pattern fixed across layers and trading little or no performance loss for significant speedups. MinkowskiEngine [15], SpConv [59], TorchSparse [50], and TorchSparse ++ [51] are some 3D point cloud engines built upon such sparse convolution for high-performance inference on GPUs.

Despite these advances, such techniques have not yet been explored in the FPGA domain, which is critical for certain scientific experiments that demand especially low latencies. Our proposed method addresses this with an implementation of sparse convolution that selectively computes only on a small subset of input pixels and achieves

constant runtime by imposing a maximum output sparsity, enabling parallel processing on FPGAs to achieve large inference speedups.

### 3 Method

We first present the background and define sparse convolution in Sec. 3.1, then lay out the algorithmic details of the HLS implementation in Sec. 3.2.

#### 3.1 Background and sparse convolution

For simplicity, *same* padding and unit stride are assumed in the rest of the paper. In a standard 2D convolutional layer, for an input tensor  $I$  with dimensions  $(H, W, C_{\text{in}})$ , an output tensor  $O$  with dimensions  $(H, W, C_{\text{out}})$ , and a kernel weight tensor  $T$  with dimensions  $(K, K, C_{\text{in}}, C_{\text{out}})$ , three nested loops are required to accumulate input-weight multiplications for each output pixel and channel [38]:

$$O[i, j, c_{\text{out}}] = b[c_{\text{out}}] + \sum_{c_{\text{in}}=0}^{C_{\text{in}}-1} \sum_{k_h=0}^{K-1} \sum_{k_w=0}^{K-1} I[i + k_h, j + k_w, c_{\text{in}}] T[k_h, k_w, c_{\text{in}}, c_{\text{out}}], \quad (1)$$

where  $b$  denotes the  $C_{\text{out}}$  bias terms, and the input indices are shifted to the proper spatial patch. Eq. 1 is computed for each output pixel ( $0 \leq i < H, 0 \leq j < W$ ) and channel ( $0 \leq c_{\text{out}} < C_{\text{out}}$ ). Thus, a standard Conv2D performs  $HWC_{\text{out}}$  inner products, each with  $C_{\text{in}}K^2$  multiplications, totaling  $HWC_{\text{out}}C_{\text{in}}K^2$  multiplications (six nested loops). Directly implementing these deep nested loops in HLS leads to high latency because each transition across loop levels, say exiting an inner loop to its enclosing outer loop or re-entering for the next iteration, costs one clock cycle, introducing loop-carried dependencies and scheduling overhead. A common workaround is to pipeline an outer loop and unroll inner loops so iterations execute in parallel, but this is infeasible for typical image sizes due to resource usage and memory bandwidth. Because of these limitations, `hls4ml` uses stream I/O to implement convolutional architectures. In stream I/O, inputs are processed sequentially via “first in, first out” (FIFO) buffers, which use fewer resources than parallel I/O. For an input of size  $H \times W \times C_{\text{in}}$ , the  $H \times W$  pixels are fed one-by-one, each carrying  $C_{\text{in}}$  features. Pixels are buffered until a full sliding window is available, then the multiply-accumulate is performed. Since streaming reads one pixel per clock, the latency is at least  $H \times W$  cycles to scan the image, plus additional cycles to fill and drain the sliding window, which scale with  $W$  and  $K$ . This approach enables large inputs but yields too high latencies for constrained systems.

For large images with spatially sparse features, implementing standard convolution is often prohibitive, or, if feasible, wastes most computation on empty regions that contain little or no semantic information and thus contribute little to feature extraction. In contrast, sparse convolution is a special (constrained) type of convolution that selectively computes on a subset of pixels instead of densely convolving the entire image. Which pixels are selected can depend on the dataset or task, but in general, selection is based on pixel activity. We consider an input pixel *active* if its feature value exceeds a predefined threshold (often zero or a small noise value). Inspired by [32], we constrain the operation so that: *an output pixel is active if and only if the input at the same pixel location is active*, and only active pixels are computed. This preserves the sparsity pattern between input and output and prevents dilation, as illustrated in Fig. 1.

Building on this sparsity-preserving convolution, we introduce the `SparsePixels` framework, which consists of five core sparse layers sufficient to build a sparse CNN: (1) sparse input reduction, (2) sparse convolution, (3) sparse activation, (4) sparse pooling, and (5) sparse flattening, illustrated in Fig. 2. The framework is designed around implementing CNNs with sparse convolution in HLS. The sparse input reduction is the first layer after the input, which extracts up to a fixed

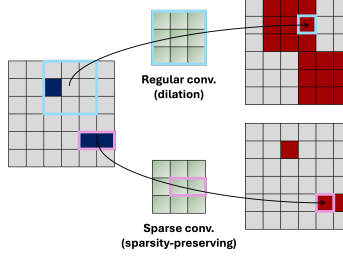


Fig. 1. Dilation of active pixels under standard convolution versus sparsity-preserving convolution, where the active set is fixed.

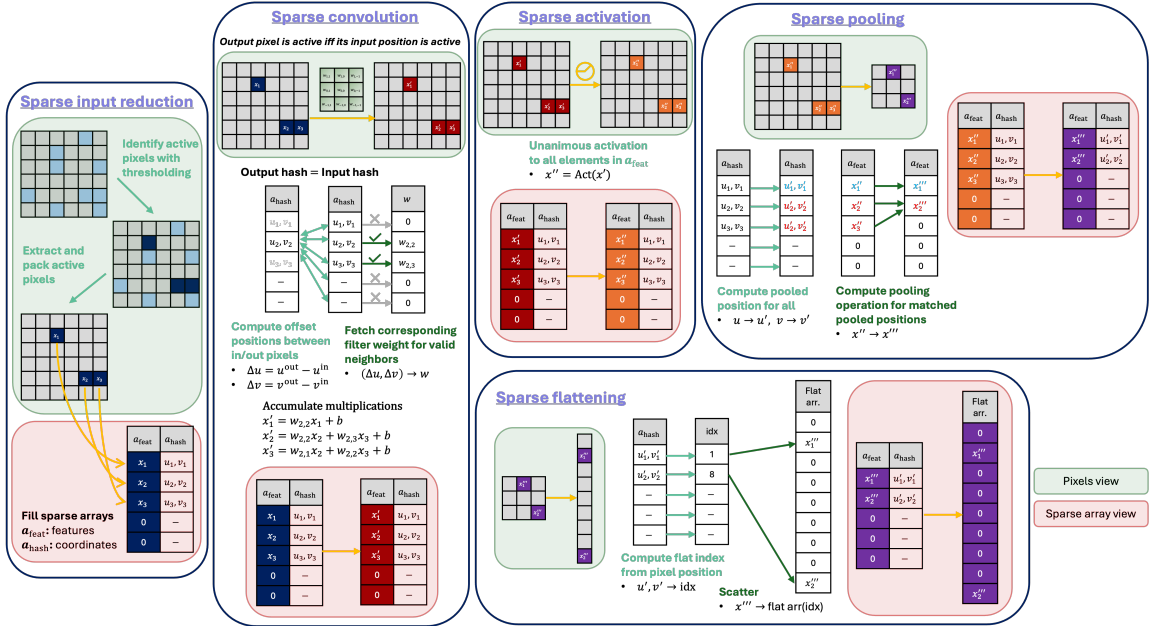


Fig. 2. Schematic diagram of SparsePixels. The framework consists of five main layers sufficient to build sparse CNNs that selectively compute on active pixels only. Sparse arrays are produced and consumed within the HLS implementation. The sparse input reduction layer dynamically retains up to  $N_{\text{active}}^{\text{max}}$  (a hyperparameter) active pixels into two sparse arrays: the feature array  $a_{\text{feat}}$  (features) and the hash array  $a_{\text{hash}}$  (height and width coordinates). The sparse convolution layer performs a sparsity-preserving convolution, updating  $a_{\text{feat}}$  while keeping  $a_{\text{hash}}$  unchanged. The sparse activation layer applies element-wise non-linearity for  $a_{\text{feat}}$ . The sparse pooling layer applies downsampling, updating both  $a_{\text{feat}}$  and  $a_{\text{hash}}$ . The sparse flattening layer transforms the sparse arrays into a flat dense array that can be connected to conventional dense layers for downstream tasks such as classification and regression.

number of active pixels from the input images and groups them for subsequent processing. The sparse convolutional layer performs a sparsity-preserving convolution that fixes the input-output sparsity. The other sparse layers retain their usual functionality but operate on the stored active pixels. For training, we have developed a Python library to build and train sparse CNNs that mirror the HLS behavior. The training library uses QKeras as a backend for QAT [18], and will support high-granularity quantization (HGQ) [49] in the future. The HLS implementation of the sparse layers is detailed in the following section.

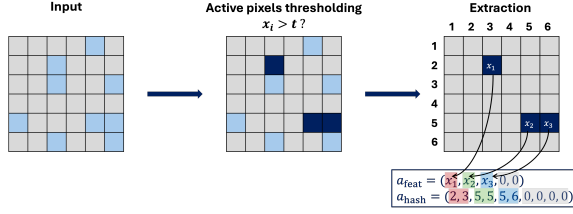


Fig. 3. Identification of active pixels through thresholding. Only active pixels are stored in the sparse arrays:  $a_{feat}$  holds features, and  $a_{hash}$  holds the corresponding height and width coordinates. The example uses  $N_{\text{sparse}} = 5$ .

### 3.2 HLS implementation

In HLS, the core idea is to store only the active pixels in compact arrays and perform all subsequent computation on these arrays.

**3.2.1 Sparse input reduction.** The first step is to read out the active pixels from the input, as illustrated in Fig. 3. For an input image with  $H \times W$  pixels and  $C$  channels, the active pixels are identified as those whose (channel-0 by convention) feature value exceeds a predefined threshold, and are extracted into two compact sparse arrays: the *feature array*  $a_{feat}$  (storing all  $C$  channel values for each retained pixel) and the *hash array*  $a_{hash}$  (storing the corresponding height and width coordinates). We fix a maximum number of active pixels per model,  $N_{\text{active}}^{\max}$ , which sets the array sizes:  $a_{feat}$  has  $N_{\text{active}}^{\max} \times C$  elements and  $a_{hash}$  has  $N_{\text{active}}^{\max} \times 2$  elements. Thus, instead of computing over all  $H \times W$  pixels as in standard convolution, we operate on arrays whose size scales with  $N_{\text{active}}^{\max} << H \times W$  for sparse data. Unlike in Python, which can allow a variable number of pixels per example, the number of active pixels to be computed must be bounded in HLS because the design is fixed once synthesized into firmware. A naive implementation, say scanning all input pixels once and “pushing” active pixels into an output array via an “if-else”, creates data-dependent write addresses, where the next write index depends on how many active pixels were seen. In HLS this induces loop-carried dependencies that can inflate scheduling and synthesis cost even when the output array is small.

To avoid data-dependent writes, we use a recursive binary reduction scheme to read out the active pixels, as illustrated in Fig. 4. Let  $N = H \times W$  and flatten the first channel into a length- $N$  array. We then split it into two partitions where the left partition has size  $2^{\lfloor \log_2(N-1) \rfloor}$  (largest power of two less than  $N$ ) and the right holds the remainder. The split recurses until we reach pairs. The reduction tree depth is therefore

$$\text{reduction tree depth} = \lceil \log_2(H \times W) \rceil. \quad (2)$$

Using a simple pairwise combiner that returns the left element if it is above threshold and otherwise the right, we reduce each level until one element remains, which is the leftmost active pixel from the flat input array. We write this pixel’s feature(s) and coordinates into the first slots of  $a_{feat}$  and  $a_{hash}$ , set its value to zero in the input array, and repeat the reduction to obtain the next leftmost active. This continues until we have filled up to  $N_{\text{active}}^{\max}$  entries. By convention, the ordering is row-major (top-left to bottom-right). This approach is hardware-efficient as it replaces the data-dependent “push-back” with a fixed-shape reduction tree. The algorithmic details are given in Alg. 1.

**3.2.2 Sparse convolution.** Next, we perform sparse convolution that takes as inputs the two sparse arrays, as illustrated in Fig. 5. Because the operation preserves the sparsity pattern, the active pixel locations are identical at input and output. Consequently, only the feature array is updated while the hash array remains unchanged.

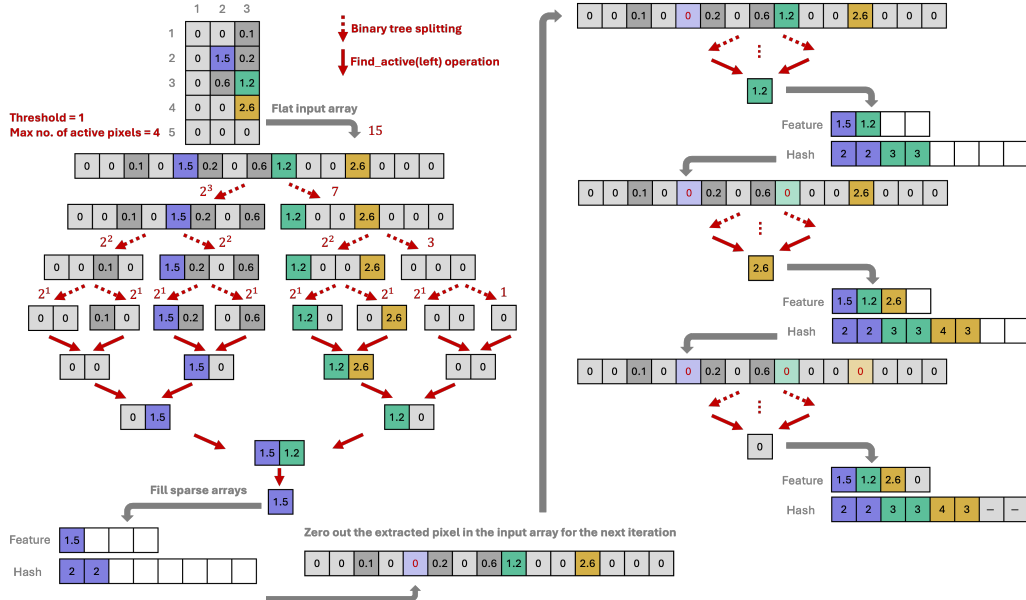


Fig. 4. Schematic diagram of the recursive tree splitting and pairwise combiner used in the sparse input reduction layer.

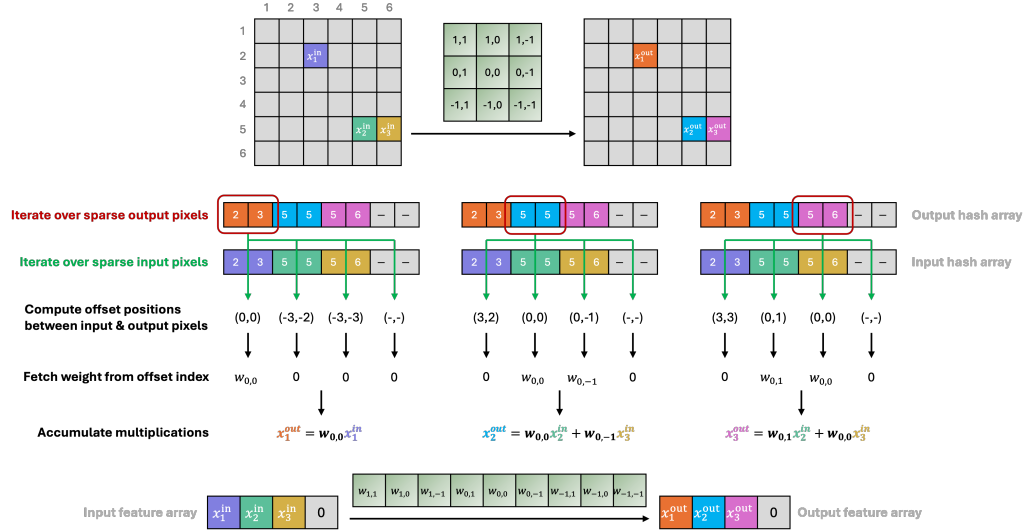


Fig. 5. Schematic diagram of sparse convolution implemented in HLS. Active pixel locations are unchanged. Only the feature array is updated.

Since only active pixels can contribute and the input and output share the same active locations, no information from inactive pixels is required. On the sparse arrays, we loop over output pixels; for each output pixel we loop over input pixels and compute the offsets ( $\Delta h, \Delta w$ ) between their coordinates from the hash array. If  $(\Delta h, \Delta w)$  lies within the  $K \times K$

**Algorithm 1:** Sparse Input Reduction in HLS

---

**Inputs** : flat channel-last input  $X[0..HWC - 1]$ , active pixel threshold  $t$ , max number of active pixels  $N_{\text{active}}^{\max}$   
**Outputs** : sparse feature array  $a_{\text{feat}}[0..N_{\text{active}}^{\max} \cdot C - 1]$ , sparse hash array  $a_{\text{hash}}[0..N_{\text{active}}^{\max} \cdot 2 - 1]$

```

1 Function OpActive( $a, b; t$ ) // a, b are pairs (getValue, getIndex):
2   if  $a.\text{getValue} > t$  then
3      $\quad \text{return } a$ 
4   else if  $b.\text{getValue} > t$  then
5      $\quad \text{return } b$ 
6   else
7      $\quad \text{return } (0, 0)$ 
8 Function FindActive( $P[0..N - 1], t$ ) // returns leftmost active by recursive reduction:
9   if  $N = 1$  then
10     $\quad \text{return } P[0]$ 
11   else if  $N = 2$  then
12     $\quad \text{return } \text{OpActive}(P[0], P[1], t)$ 
13   else
14      $N_{\text{left}} \leftarrow 2^{\lfloor \log_2(N-1) \rfloor}$  // largest power-of-two < N
15      $u \leftarrow \text{FindActive}(P[0..N_{\text{left}} - 1], t)$ 
16      $v \leftarrow \text{FindActive}(P[N_{\text{left}}..N - 1], t)$ 
17      $\text{return } \text{OpActive}(u, v, t)$ 
18 Procedure SparseInputReduce // keep up to  $N_{\text{active}}^{\max}$  active pixels by scanning channel-0:
19   for  $j \leftarrow 0$  to  $HW - 1$  do
20      $P[j].\text{getValue} \leftarrow X[C \cdot j]; P[j].\text{getIndex} \leftarrow j$  // prepare channel-0 data for scan
21      $h[j] \leftarrow \text{height for } j\text{-th pixel}; w[j] \leftarrow \text{width for } j\text{-th pixel}$ 
22   for  $i \leftarrow 0$  to  $N_{\text{active}}^{\max} - 1$  do
23      $p \leftarrow \text{FindActive}(P[0..HW-1], t)$ 
24      $a_{\text{feat}}[C \cdot i] \leftarrow p.\text{getValue}$  // fill feature for first channel
25     for  $c \leftarrow 1$  to  $C - 1$  do
26        $a_{\text{feat}}[C \cdot i + c] \leftarrow X[C \cdot p.\text{getIndex} + c]$  // fill feature for other channels
27      $a_{\text{hash}}[2i] \leftarrow h[p.\text{getIndex}]$  // fill height
28      $a_{\text{hash}}[2i + 1] \leftarrow w[p.\text{getIndex}]$  // fill width
29      $P[p.\text{getIndex}].\text{getValue} \leftarrow 0$  // after consume, mask to reveal the next active

```

---

receptive field, we map that offset to the corresponding kernel position and accumulate a channel-wise dot product between the input features and the appropriate weights; otherwise, the pair contributes nothing. By construction, if an output location is inactive (padded), it will never get activated in subsequent layers.

For each output channel, the sparse convolution involves two nested loops over active pixels (outer: output active pixels; inner: input active pixels). Because multiplications are based on an offset check and weight lookup, we do not loop over all  $K^2$  kernel positions explicitly, hence the iteration count does not scale with the kernel size. This is advantageous for sparse data, since active pixels can be far apart, and increasing  $K$  to allow long-range interactions does not increase the number of loop iterations. The relative multiply-accumulate cost between standard and sparse convolutions can be seen as:

$$\frac{N_{\text{active}}^{\max} \times N_{\text{active}}^{\max} \times C_{\text{in}} \times C_{\text{out}} \text{ (sparse conv.)}}{H \times W \times C_{\text{in}} \times C_{\text{out}} \times K \times K \text{ (standard conv.)}} \ll 1, \quad (3)$$

whenever  $N_{\text{active}}^{\max} \times N_{\text{active}}^{\max} \ll H \times W$ . The algorithmic details are given in Alg. 2.

**Algorithm 2:** Sparse 2D Convolution in HLS

---

**Inputs** :sparse feature array  $a_{\text{feat}}^{\text{in}}[0..N_{\text{active}}^{\text{max}} \cdot C_{\text{in}} - 1]$ , sparse hash array  $a_{\text{hash}}[0..N_{\text{active}}^{\text{max}} \cdot 2 - 1]$ , weights  $W[0..K^2 C_{\text{in}} C_{\text{out}} - 1]$ , bias  $b[0..C_{\text{out}} - 1]$ , odd kernel size  $K$   
**Outputs** :sparse feature array  $a_{\text{feat}}^{\text{out}}[0..N_{\text{active}}^{\text{max}} \cdot C_{\text{out}} - 1]$ , *same*  $a_{\text{hash}}$  // unchanged active pixel set

---

**1 Function**  $\text{MultAtOffset}(\Delta h, \Delta w, c_{\text{out}}, p_{\text{in}})$  // Mult-accum based on offset in  $K^2$  field:

2     $R \leftarrow (K - 1)/2$   
3    **if**  $|\Delta h| > R$  **or**  $|\Delta w| > R$  **then**  
4     **return** 0 // offset is outside kernel field  
5    **else**  
6     **map offset to weight array index**  
7      $pos \leftarrow (R - \Delta h) \cdot K + (R - \Delta w)$  // flattened spatial position  $0..K^2 - 1$   
8      $w_{\text{idx}} \leftarrow C_{\text{out}} \cdot C_{\text{in}} \cdot pos + C_{\text{in}} \cdot C_{\text{out}}$  // weight array ordering: pixel\_pos → ch\_out → ch\_in  
9      $M \leftarrow 0$   
10    **for**  $c_{\text{in}} \leftarrow 0$  **to**  $C_{\text{in}} - 1$  **do**  
11      $M \leftarrow M + W[w_{\text{idx}} + c_{\text{in}}] \cdot a_{\text{feat}}^{\text{in}}[C_{\text{in}} \cdot p_{\text{in}} + c_{\text{in}}]$  // dot over input channels  
12    **return**  $M$

---

**12 Procedure**  $\text{SparseConv}$  // convolve on sparse arrays ( $N_{\text{active}}^{\text{max}} \cdot N_{\text{active}}^{\text{max}} \cdot C_{\text{in}} \cdot C_{\text{out}}$  total iterations):

13    **loop over output pixels**  
14    **for**  $p_{\text{out}} \leftarrow 0$  **to**  $N_{\text{active}}^{\text{max}} - 1$  **do**  
15     **loop over output channels**  
16     **for**  $c_{\text{out}} \leftarrow 0$  **to**  $C_{\text{out}} - 1$  **do**  
17        $A \leftarrow 0$   
18       **loop over input pixels**  
19       **for**  $p_{\text{in}} \leftarrow 0$  **to**  $N_{\text{active}}^{\text{max}} - 1$  **do**  
20          $\Delta h \leftarrow a_{\text{hash}}[2p_{\text{out}}] - a_{\text{hash}}[2p_{\text{in}}]$  // compute offset in height  
21          $\Delta w \leftarrow a_{\text{hash}}[2p_{\text{out}} + 1] - a_{\text{hash}}[2p_{\text{in}} + 1]$  // compute offset in width  
22          $A \leftarrow A + \text{MultAtOffset}(\Delta h, \Delta w, c_{\text{out}}, p_{\text{in}})$  // offset-based mult-accum  
23          $A \leftarrow A + b[c_{\text{out}}]$   
24         **if** pixel  $p_{\text{out}}$  is padded **then**  
25            $A \leftarrow 0$   
26          $a_{\text{feat}}^{\text{out}}[C_{\text{out}} \cdot p_{\text{out}} + c_{\text{out}}] \leftarrow A$

---

**3.2.3 Sparse activation.** As in standard activation, sparse activation applies an element-wise nonlinearity to the sparse feature array while keeping the hash array unchanged. The number of elements processed is greatly reduced:

$$\frac{N_{\text{active}}^{\text{max}} \times C \text{ (sparse act.)}}{H \times W \times C \text{ (standard act.)}} \ll 1, \quad (4)$$

whenever  $N_{\text{active}}^{\text{max}} \ll H \times W$ . The algorithmic details are given in Alg. 3.

**3.2.4 Sparse pooling.** For sparse pooling, we first map every retained pixel's coordinate in the sparse array to its pooled coordinates and write into a new hash array to reflect the downsampled sparsity pattern. We then loop over pooled pixel positions and accumulate features from pixels that land in the same pool, finally applying the pooling operation. The algorithmic details are given in Alg. 4.

**3.2.5 Sparse flattening.** All sparse layers above compute on and output sparse arrays that represent a reduced representation of the original image. Before connecting to conventional dense layers for downstream tasks, we transform back to a flat dense representation. We first initialize a flat dense array with zeros, then map the coordinate of each retained pixel to the corresponding index and scatter its  $C$  channel features to the corresponding slots. The algorithmic details are given in Alg 5.

## 4 Evaluations

We perform scaling studies for the five sparse layers to understand their latency and resource utilization on an FPGA by scanning key hyperparameters, as presented in Sec. 4.1. We then perform experiments to evaluate sparse CNNs on an FPGA comparing against standard CNN baselines on three datasets in Sec. 4.2: the datasets are described in Sec. 4.2.1, the experimental setup in Sec. 4.2.2, and the results in Sec. 4.2.3.

### 4.1 Scaling studies

In the scaling studies, layers are synthesized with Vitis HLS (2023.1) [9], targeting an AMD/Xilinx Alveo FPGA with part number xcu250-fgd2104-2L-e. We report FPGA resource utilization from the HLS compilation step (C-synthesis results), which typically provides conservative estimates (overestimation). We quote C-synthesis numbers here rather than logic synthesis because we are characterizing individual layers: logic synthesis can allocate a non-negligible fraction of resources into shared FIFO buffers across layers, which could lead to double-counting if quoted per layer. We report latency in clock cycles, using a 200 MHz clock (a standard benchmark for `hls4ml` and deployments at the LHC), and utilization for four resource types: block random access memory (BRAM), digital signal processor (DSP), flip-flop (FF), and look-up table (LUT). Utilization is given as a percentage relative to the total available on the target device: BRAMs=5,376, DSPs=12,288, FFs=3,456,000, and LUTs=1,728,000.

For the sparse input reduction layer, we test six input sizes: 500, 1000, 1500, 2000, 2500, and 3000 pixels. For each input size, we scan  $N_{\text{active}}^{\max}$  from 5 to 30 in steps of 5. The latency and resource utilization are shown in Fig. 6. Latency scales linearly with  $N_{\text{active}}^{\max}$  across input sizes because the outer loop iterates over the retained active pixels. The latency curves for 500/1000/1500/2000 pixels coincide and differ from 2500/3000, reflecting the stepwise behavior of the reduction tree depth in Eq. 2 (Sec. 3.2.1). No DSPs are required because the readout involves only comparisons and data moves. FF/LUT usage is nearly flat versus  $N_{\text{active}}^{\max}$  for a fixed input size, dominated by the fixed reduction-tree width, and increases with input size or bit width.

For the sparse convolutional layer, we evaluate  $(C_{\text{in}}, C_{\text{out}}) \in \{(1, 1), (1, 3), (2, 1), (2, 2), (3, 1), (3, 3)\}$ , kernel sizes  $K \in \{3, 5\}$ , and  $N_{\text{active}}^{\max}$  from 5 to 30 in steps of 5. We choose a small number of input/output channels because spatially sparse inputs typically exhibit simpler semantic patterns, so compact models suffice for low-latency applications and can achieve performance comparable to standard CNNs (see Sec. 4.2.3). In addition, fully parallel implementations with many filters often incur prohibitive resource usage on an FPGA. Exploring larger numbers of filters is more appropriate once the framework is extended with a streaming implementation in the future. Latencies are shown in Fig. 7 and resource utilization in Fig. 8. Full or partial parallelization of standard convolution at these input sizes is beyond the capabilities of the current `hls4ml` implementation, so we do not include it. Latency and resource usage are broadly similar for  $K = 3$  and  $K = 5$ , except that the latter can require more BRAMs to store larger weight tensors as channels increase. This matches the design in Sec. 3.2.2: the number of iterations does not scale with  $K$  because kernel positions are accessed via offset checks rather than explicit loops over all  $K^2$  positions. In our tested configurations, the total number of iterations is small enough to fully unroll the loops, yielding very low latency at the cost of higher resource usage. As  $C_{\text{in}}$ ,  $C_{\text{out}}$ , or  $N_{\text{active}}^{\max}$  grows, the degree of parallelism increases and so do resources.

Scaling results for sparse activation are presented in Sec. A.1, sparse pooling in Sec. A.2, and sparse flattening in Sec. A.3.

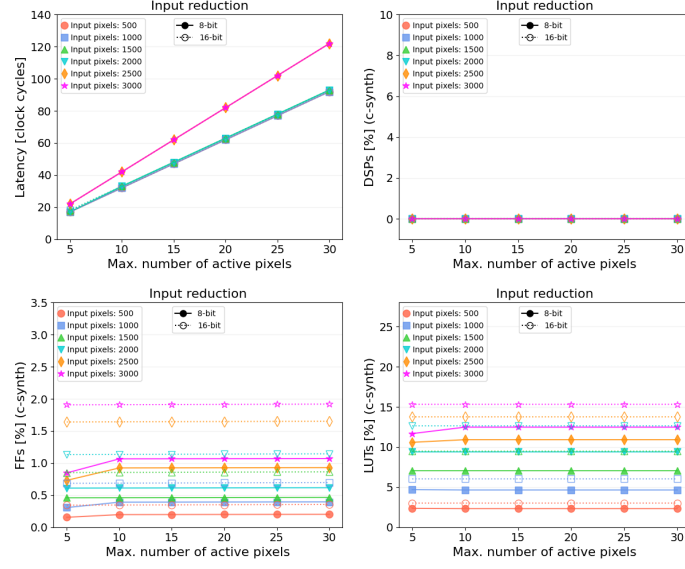


Fig. 6. Scaling of the sparse input reduction layer for different input sizes and  $N_{\text{active}}^{\max}$ : latency (upper left), DSPs (upper right), FFs (lower left), and LUTs (lower right). Resource utilization is obtained from the HLS C-synthesis step.

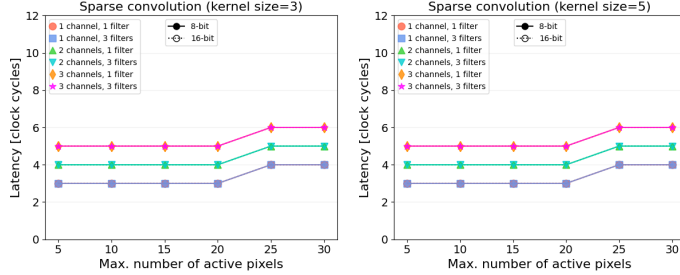


Fig. 7. Latency scaling of the sparse convolutional layer for varying channels and  $N_{\text{active}}^{\max}$ . Two kernel sizes are shown:  $K = 3$  (left) and  $K = 5$  (right). Loops are fully unrolled.

## 4.2 Evaluation on relevant datasets

**4.2.1 Datasets.** We perform experiments on three datasets with sparse image data: handwritten digits, neutrino detection in the MicroBooNE experiment, and jet flavor tagging at the LHC. The datasets and preprocessing are described below.

We first inspect a toy dataset derived from MNIST [39]. The original images have  $28 \times 28$  pixels and are already somewhat sparse, but we target sparsity at the few-percent level or below. For demonstration, we further sparsify the features with the following transformations: (1) apply average pooling with pool size 3 to reduce the number of nonzeros; (2) zero-pad the boarders to resize to  $48 \times 48$ ; (3) radially “inflate” pixels outward proportional to their distance from the image center, so the active pixels are more separated spatially (this avoids over-compression by later pooling); (4) zero out low-valued pixels with a threshold at 0.4. An example image is shown in Fig. 9. The task we

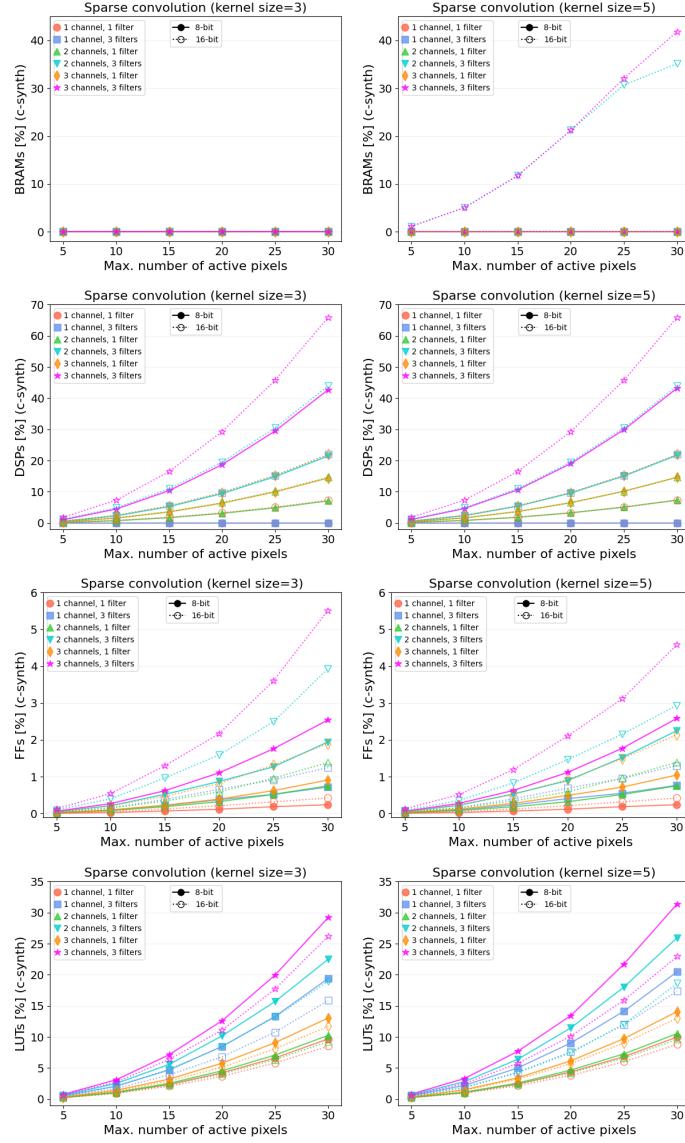


Fig. 8. Resource scaling of the sparse convolutional layer for varying channels and  $N_{\text{active}}^{\max}$ : BRAMs (row 1), DSPs (row 2), FFs (row 3), and LUTs (row 4). Two kernel sizes are shown:  $K = 3$  (left) and  $K = 5$  (right). Loops are fully unrolled. Resource utilization is obtained from the HLS C-synthesis step.

consider is supervised multi-class classification of the processed images. We also illustrate the importance of choosing a proper  $N_{\text{active}}^{\max}$ , a hyperparameter of our sparse CNNs (and a fixed bound in HLS). As described in Sec. 3.2.1,  $N_{\text{active}}^{\max}$  caps the number of active pixels retained in sparse arrays which are subsequently processed by sparse convolution. Pixels are scanned in a row-major order (top left to bottom right). A larger  $N_{\text{active}}^{\max}$  preserves more information but increases hardware cost, whereas too small a value leads to semantic information loss in a way that depends on the

Manuscript submitted to ACM

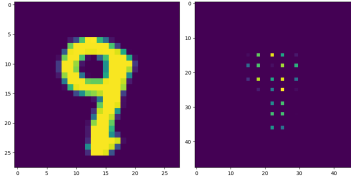


Fig. 9. Example MNIST image before (left) and after (right) preprocessing.

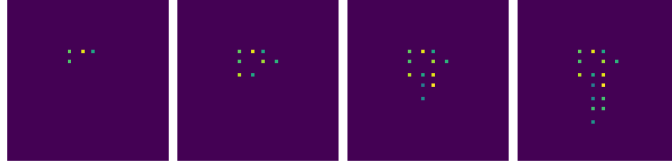


Fig. 10. Effect of  $N_{\text{active}}^{\text{max}}$  on retained semantics. From left to right:  $N_{\text{active}}^{\text{max}} = 4, 8, 12, 16$ .

spatial sparsity of a given dataset. In Fig. 10, using the digit “9” as an example,  $N_{\text{active}}^{\text{max}} = 4$  is insufficient to resemble any class; 8 captures only the upper half which resembles the digit “0”; 12 begins to include the lower part; and 16 recovers the full “9”. Thus an  $N_{\text{active}}^{\text{max}}$  scan is necessary to balance accuracy and hardware cost for a given dataset.

Next, we consider a realistic neutrino dataset from MicroBooNE Open Samples [5, 6, 8]. MicroBooNE uses a liquid argon time projection chamber (LArTPC) to record neutrino interaction events. In a LArTPC, an incoming neutrino (or a cosmic-ray particle) interacts with an argon nucleus, producing charged particles that ionize argon along their trajectories. Ionization electrons drift to the anode under an applied electric field and induce signals on wire sensor planes. The arrival time and wire position are used to reconstruct 2D images containing particle trajectories. The dataset we use contains simulated neutrino interactions overlaid on real cosmic-ray background. Originally, each LArTPC image has 6400 time bins and 3456 wire bins (or 2400, depending on plane), and pixel values are sensor amplitudes. An example is shown at the top of Fig. 11, where the time axis is compressed by a factor of 6, and the pixel intensity is saturated at 100 and cut at 10. The objective is to detect whether an image contains a neutrino interaction. We extract windows of size  $256 \times 512$ , which are large enough to contain nearly all of the activity from a neutrino interaction. Windows containing a simulated neutrino interaction (based on truth labels) are labeled as signal, while background windows are randomly cropped elsewhere. To make the computation manageable, we downsample the windows to  $63 \times 63$  by summing the bins, then denoise by zeroing pixels below 700, as shown in Fig. 11. Signal windows tend to contain intersecting tracks forming a vertex while background windows contain fewer active pixels or disconnected tracks with low intensity. Finally, features are normalized by a factor of 3200 to unit order. The task we consider is supervised binary classification.

Lastly, we consider jet flavor tagging at the LHC [25, 43, 45]. In proton-proton collisions, unstable heavy particles are produced and they decay promptly into sprays of particles recorded by the detector. When the parent particle has high momentum, the constituent particles appear as a collimated cone, called a jet. Jet substructure (particle content, energy, and geometry) encodes the identity of the parent particle, and identifying the originating particle is called jet tagging. The dataset we use contains simulated jets with transverse momentum ( $p_T$ ) around 1 TeV produced from proton-proton collisions at the center-of-mass energy of 13 TeV. Jets are clustered with the anti- $k_T$  algorithm [13] using the distance parameter at  $R = 0.8$ . Five jet classes are simulated: gluon (g), light quark (q), W boson, Z boson, and top

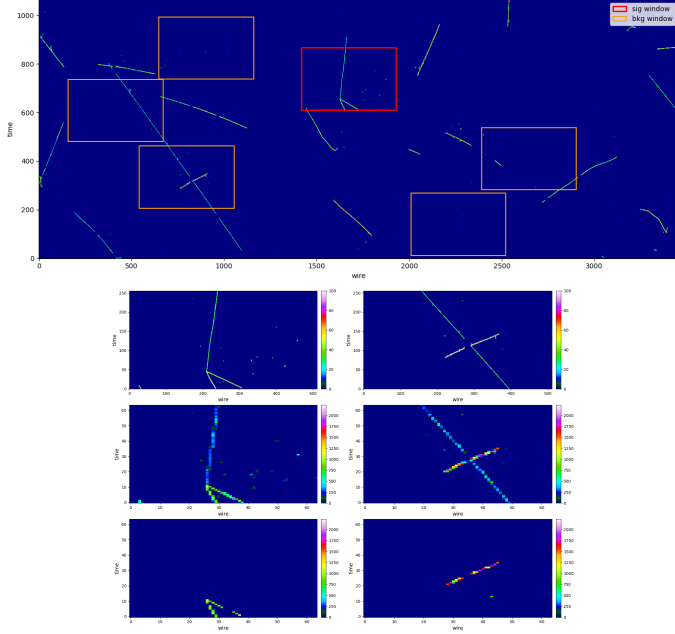


Fig. 11. Example MicroBooNE neutrino image. Top: original view with signal (red) and background (orange) windows indicated. Bottom:  $256 \times 512$  windows downsampled to  $63 \times 63$  and denoised by thresholding.

quark (t). Each jet is represented as a  $100 \times 100$  image in pseudorapidity  $\eta$  (transformed polar angle) and azimuthal angle  $\phi$  relative to the jet axis; each pixel stores the scalar sum of particle  $p_T$  measured in calorimeters, and up to the 150 highest- $p_T$  constituents per jet are retained. Example images are shown in the top row of Fig. 12. The task we consider is supervised multi-class classification of the processed images. Because the original images are too large for full parallelization on an FPGA, we preprocess the images for demonstration: (1) crop from  $100 \times 100$  to  $56 \times 56$  by removing border pixels; (2) normalize pixel values by a factor of 1200, saturate at 1, and cut at 0.003 (middle row in Fig. 12); (3) as with MNIST, apply radial inflation to spread active pixels outward from the center so that subsequent pooling does not collapse information (bottom row in Fig. 12).

**4.2.2 Experimental setup.** For a fair comparison, we use the same base architecture to construct both the standard CNN and the sparse CNN in each experiment. The three models, one for each dataset experiment, are shown in Fig. 13. Each model consists of two convolution blocks (a convolutional layer followed by ReLU), uses average pooling for downsampling, then flattens to feed a two-layer multilayer perceptron (MLP) classifier. These models are compact (approx. 4k parameters), as is typical for low-latency FPGA applications. The only architectural difference between the standard and sparse models is that the sparse CNN computes on at most  $N_{\text{active}}^{\max}$  pixels. For the sparse CNNs, we test  $N_{\text{active}}^{\max} \in \{8, 12, 16, 20\}$ , referred to as *tiny, small, medium, large*. We compare accuracy and FPGA cost between the standard CNN and these sparse variants, training with our `SparsePixels` library using QKeras for quantization-aware training, evaluating two fixed total bit-widths: 8 and 16.

For MNIST, we use the 70k examples split into 50k/10k/10k for train/val/test. Models are trained with batch size 128 for up to 200 epochs with early stopping, using Adam [37] with a learning rate of  $10^{-3}$  to optimize categorical

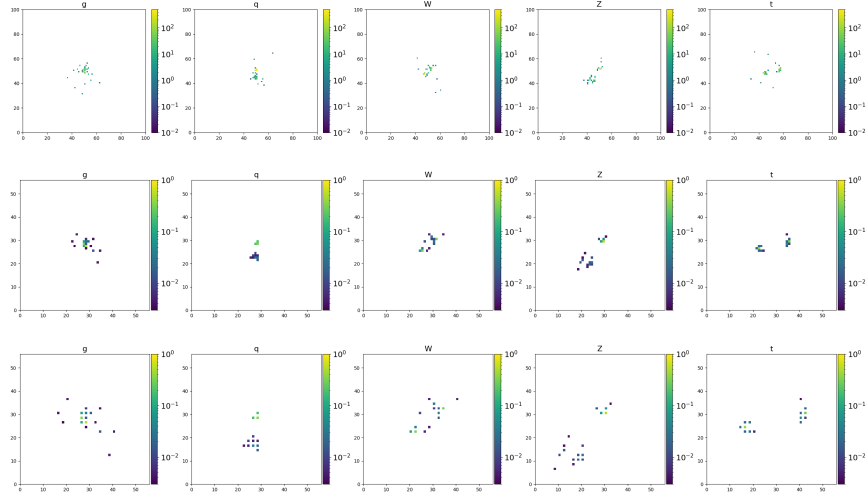


Fig. 12. Example jet images for classes g, q, W, Z, and t (left to right). Top: original  $100 \times 100$  images. Middle: pooled and padded to  $56 \times 56$  with low-energy hits zeroed. Bottom: sparsified by radial inflation.

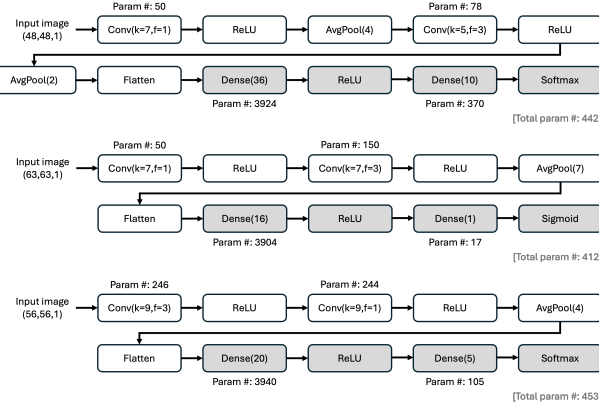


Fig. 13. Base architectures for constructing both standard and sparse CNNs for the MNIST (top), neutrino (middle), and jet tagging (bottom) experiments. All have two convolutional blocks followed by a 2-layer MLP, with a compact model size of around 4k parameters.

cross-entropy. For MicroBooNE dataset, we use 160k windows with balanced signal and background, split 70/10/20% for train/val/test. Training settings are the same as for MNIST except the loss is binary cross-entropy. For the LHC jet dataset, we use 300k jets split 70/10/20% for train/val/test sets, with the same training settings as for MNIST.

After training, we generate HLS for all models with `hls4ml` [2, 25, 26]. Standard CNNs are implemented with stream I/O (they are too large with parallel I/O) and synthesized with Vivado HLS (2020.1) [58], the currently stable version for convolutional architectures. Sparse CNNs use parallel I/O and are synthesized with Vitis HLS (2023.1) [9]. The reported resources are obtained after the logic synthesis step. Same as in the scaling studies, the target device is an AMD/Xilinx Alveo FPGA with part number xcu250-figd2104-2L-e, and the clock frequency is set to 200 MHz (5 ns clock period).

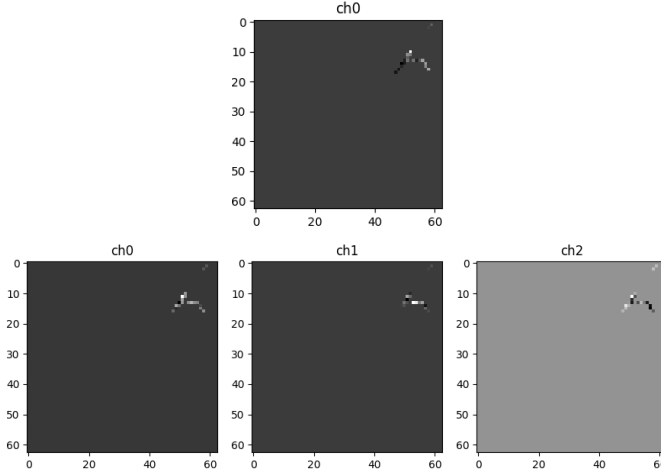


Fig. 14. Illustration of sparse convolution on an example neutrino image from the MicroBooNE dataset. Top: single-channel input. Bottom: three output channels after one sparse convolution.

**4.2.3 Results.** Fig. 14 illustrates sparse convolution on an example neutrino signal image from the MicroBooNE dataset, showing the input and the output after one sparse convolutional layer. As designed, the active pixel locations are unchanged. Sparse convolution is a constrained operation, where feature updates occur only at active pixels. This limits the spread of information to neighboring locations and narrows how pixels communicate across layers. Since the number of active pixels never increases (sparse convolution preserves the active set and pooling typically reduces it), one can trade computation for accuracy by increasing the number of output channels per layer. Likewise, a larger kernel can increase the receptive field among active pixels, as our HLS implementation does not directly scale the iteration count with the kernel size (see Sec. 3.2.2).

Fig. 15 shows model performance. As expected, sparse CNN accuracy improves with larger  $N_{\text{active}}^{\max}$  because more semantic information is retained. The sparse-large models ( $N_{\text{active}}^{\max} = 20$ ) are the most accurate among the sparse variants and are close to the standard CNNs. A small performance loss is expected, since sparse CNNs compute on a subset of pixels and enforce a sparsity-preserving convolution, but these small losses are traded for significant FPGA inference speedups.

Tab. 1 summarizes latency, speedup, and performance relative to the standard CNNs. Across all datasets, sparse-large gains more than an order-of-magnitude speedup with comparable or slightly lower accuracy. The high latency of standard CNNs comes from computing on all pixels and, given the large image sizes, the need to use stream I/O (one pixel streaming per cycle plus additional buffering). In contrast, sparse CNNs selectively compute on a small fraction of pixels, for example, on MicroBooNE, sparse-large consumes 20 of  $63 \times 63$  input pixels (0.5%), and the compact representation enables parallel processing on FPGA, where all active pixels can be processed concurrently. Concretely, for MicroBooNE, sparse-large at 8-bit achieves a  $\times 73$  speedup over the 8-bit standard CNN (133 vs. 9733 clock cycles, i.e., 0.665 vs. 48.665  $\mu$ s) with < 2% ROC AUC drop (0.927 vs. 0.943). Similar results are observed for the other datasets.

For all sparse CNNs, the initiation interval (II)—the number of clock cycles between accepting successive inputs—equals the latency of the sparse input reduction layer (the first layer in sparse models), which can be seen in the per-layer latency breakdown in Fig. 17 (8-bit) and Fig. 22 (16-bit). This is because the recursive tree splitting requires

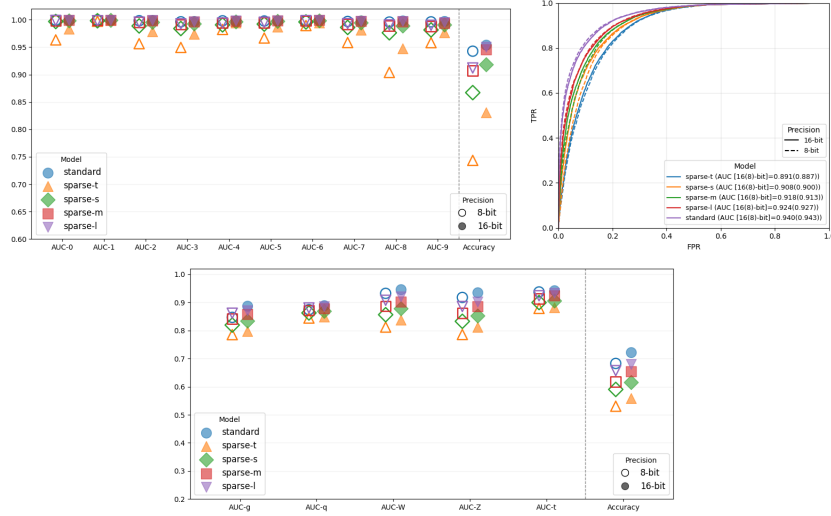


Fig. 15. Model performance comparing the standard CNNs and the sparse CNNs for MNIST (upper left), neutrino (upper right), and jet tagging (lower).

buffering and processing the current input array until scanning completes before the next array can enter. Subsequent sparse layers operate on sparse arrays and their operations are maximally parallelized.

Fig. 16 (Fig. 21) shows resource usage as a fraction of the total available on device for 8-bit (16-bit) models. As discussed, standard CNNs, implemented with stream I/O, tend to use fewer resources due to sequential processing, while sparse CNNs, implemented with parallel I/O, consume more resources in exchange for much lower latency. For example, LUT usage is several times higher in sparse CNNs because loops are largely unrolled to execute concurrently. This increase is less concerning since even the sparse-large models consume only  $O(20\%)$  of total LUTs on device, but this is traded for much larger speedups. When needed, reuse factors—an HLS setting that controls parallelization by having a processing element perform more sequential operations—can be increased for the sparse CNNs to reduce resources at the cost of higher latency, a trade-off that is acceptable given the currently seen substantial baseline speedups. Per-layer resource breakdowns shown in Fig. 17 Fig. 22 are consistent with the scaling behaviors in Sec. 4.1.

## 5 Summary

We have introduced **SparsePixels**, a framework for sub-microsecond FPGA inference of CNNs using sparse convolution on spatially sparse 2D data. The key features in our HLS implementation are: (1) dynamically identifying and packing active pixels, a small subset of a large input, into compact arrays, then (2) performing all subsequent computation only on those packed pixels while ignoring inactive pixels. By selectively computing on the necessarily informative subset, the design avoids computation on empty regions, yielding significant inference speedups and resource savings, especially when only percent-level or fewer pixels are active. As a representative example on MicroBooNE neutrino images with 4000 input pixels, a sparse CNN that computes on at most 20 active pixels achieves a  $\times 73$  inference speedup on an FPGA over a standard CNN with the same base architecture (133 vs. 9733 clock cycles; 0.665 vs. 48.665  $\mu$ s), with  $< 2\%$  ROC AUC drop, and resource utilization well within device budgets (e.g., on the order of 20% LUTs for the largest sparse configuration). For easy adoption, we provide a Python library supporting quantization-aware training of sparse

Table 1. Comparison of FPGA latency and model performance between standard and sparse CNNs. The sparse- $\{t,s,m,l\}$  variants correspond to  $N_{\text{active}}^{\text{max}} = \{8, 12, 16, 20\}$ . Latency and II are measured in clock cycles (cc) with 5 ns clock period. Speedups for sparse CNNs are measured with respect to the standard CNN at the same total bit-width.

Sparse MNIST, 10 classes, 48 × 48 = 2304 input pixels														
CNN model	Latency [cc]	Speedup	II [cc]	Acc. [%]	AUC(0)	AUC(1)	AUC(2)	AUC(3)	AUC(4)	AUC(5)	AUC(6)	AUC(7)	AUC(8)	AUC(9)
Sparse-t 8b	79 (0.395 $\mu$ s)	$\times 41$	35 (0.175 $\mu$ s)	74.3	0.9631	0.9972	0.9562	0.9494	0.9822	0.9666	0.9893	0.9583	0.9038	0.9581
Sparse-t 16b	81 (0.405 $\mu$ s)	$\times 40$	35 (0.175 $\mu$ s)	83.1	0.9834	0.9990	0.9788	0.9735	0.9941	0.9872	0.9948	0.9817	0.9476	0.9770
Sparse-s 8b	104 (0.52 $\mu$ s)	$\times 31$	52 (0.26 $\mu$ s)	86.7	0.9967	0.9981	0.9886	0.9839	0.9906	0.9920	0.9959	0.9859	0.9762	0.9813
Sparse-s 16b	106 (0.53 $\mu$ s)	$\times 30$	52 (0.26 $\mu$ s)	91.8	0.9987	0.9994	0.9956	0.9922	0.9969	0.9971	0.9982	0.9943	0.9893	0.9908
Sparse-m 8b	124 (0.62 $\mu$ s)	$\times 26$	67 (0.335 $\mu$ s)	90.7	0.9984	0.9987	0.9956	0.9914	0.9942	0.9946	0.9980	0.9919	0.9892	0.9882
Sparse-m 16b	127 (0.635 $\mu$ s)	$\times 25$	67 (0.335 $\mu$ s)	94.6	0.9994	0.9996	0.9984	0.9963	0.9978	0.9983	0.9991	0.9975	0.9966	0.9940
Sparse-l 8b	146 (0.73 $\mu$ s)	$\times 22$	84 (0.42 $\mu$ s)	91.2	0.9988	0.9982	0.9957	0.9925	0.9942	0.9955	0.9984	0.9929	0.9906	0.9899
Sparse-l 16b	150 (0.75 $\mu$ s)	$\times 22$	84 (0.42 $\mu$ s)	95.0	0.9991	0.9997	0.9989	0.9969	0.9987	0.9979	0.9991	0.9971	0.9974	0.9952
Standard 8b	3232 (16.16 $\mu$ s)	—	3124 (15.62 $\mu$ s)	94.3	0.9991	0.9997	0.9982	0.9962	0.9980	0.9977	0.9985	0.9968	0.9958	0.9961
Standard 16b	3232 (16.16 $\mu$ s)	—	3124 (15.62 $\mu$ s)	95.4	0.9996	0.9997	0.9989	0.9978	0.9988	0.9981	0.9989	0.9985	0.9979	0.9976

MicroBooNE neutrino detection, 2 classes, 63 × 63 = 3969 input pixels										
CNN model	Latency [cc]	Speedup	II [cc]	$\epsilon_b$ ( $\epsilon_b = 0.2$ )	AUC					
Sparse-t 8b	69 (0.345 $\mu$ s)	$\times 141$	35 (0.175 $\mu$ s)	0.819	0.887					
Sparse-t 16b	71 (0.355 $\mu$ s)	$\times 137$	35 (0.175 $\mu$ s)	0.830	0.891					
Sparse-s 8b	90 (0.45 $\mu$ s)	$\times 108$	52 (0.26 $\mu$ s)	0.856	0.900					
Sparse-s 16b	94 (0.47 $\mu$ s)	$\times 104$	52 (0.26 $\mu$ s)	0.864	0.908					
Sparse-m 8b	111 (0.555 $\mu$ s)	$\times 88$	67 (0.335 $\mu$ s)	0.879	0.913					
Sparse-m 16b	116 (0.58 $\mu$ s)	$\times 84$	67 (0.335 $\mu$ s)	0.881	0.918					
Sparse-l 8b	133 (0.665 $\mu$ s)	$\times 73$	84 (0.42 $\mu$ s)	0.896	0.927					
Sparse-l 16b	136 (0.68 $\mu$ s)	$\times 72$	84 (0.42 $\mu$ s)	0.894	0.924					
Standard 8b	9733 (48.665 $\mu$ s)	—	5029 (25.145 $\mu$ s)	0.921	0.943					
Standard 16b	9736 (48.68 $\mu$ s)	—	5029 (25.145 $\mu$ s)	0.921	0.940					

LHC jet tagging, 5 classes, 56 × 56 = 3136 input pixels									
CNN model	Latency [cc]	Speedup	II [cc]	Acc. [%]	AUC(g)	AUC(q)	AUC(W)	AUC(Z)	AUC(t)
Sparse-t 8b	75 (0.375 $\mu$ s)	$\times 112$	35 (0.175 $\mu$ s)	53.0	0.7853	0.8443	0.8122	0.7858	0.8787
Sparse-t 16b	78 (0.39 $\mu$ s)	$\times 108$	35 (0.175 $\mu$ s)	55.8	0.7976	0.8494	0.8388	0.8117	0.8822
Sparse-s 8b	97 (0.485 $\mu$ s)	$\times 86$	52 (0.26 $\mu$ s)	59.0	0.8195	0.8626	0.8563	0.8328	0.8996
Sparse-s 16b	101 (0.505 $\mu$ s)	$\times 83$	52 (0.26 $\mu$ s)	61.5	0.8340	0.8685	0.8779	0.8529	0.9053
Sparse-m 8b	119 (0.595 $\mu$ s)	$\times 71$	67 (0.335 $\mu$ s)	61.8	0.8418	0.8722	0.8866	0.8619	0.9130
Sparse-m 16b	120 (0.6 $\mu$ s)	$\times 70$	67 (0.335 $\mu$ s)	65.5	0.8580	0.8786	0.9029	0.8856	0.9238
Sparse-l 8b	140 (0.7 $\mu$ s)	$\times 60$	84 (0.42 $\mu$ s)	65.7	0.8617	0.8805	0.9077	0.8856	0.9238
Sparse-l 16b	143 (0.715 $\mu$ s)	$\times 59$	84 (0.42 $\mu$ s)	68.1	0.8710	0.8852	0.9208	0.9032	0.9328
Standard 8b	8390 (41.95 $\mu$ s)	—	4340 (21.7 $\mu$ s)	68.3	0.8468	0.8743	0.9324	0.9178	0.9374
Standard 16b	8390 (41.95 $\mu$ s)	—	4340 (21.7 $\mu$ s)	72.2	0.8874	0.8893	0.9463	0.9361	0.9426

CNNs and HLS C++ modules for FPGA deployment. Future directions include implementing sparse layers with stream I/O, exploring partial parallelization, and integrating the framework with high-granularity quantization. We hope this work benefits experiments operating under stringent sub-microsecond latency constraints, such as modern particle experiments, where standard CNNs are often infeasible due to too high a latency and would otherwise force substantial performance compromises.

### Acknowledgments

DR is supported by the U.S. Department of Energy (DOE), Office of Science, Office of High Energy Physics Early Career Research program under Award No. DE-SC0025324. PH is supported by the U.S. National Science Foundation (NSF) Harnessing the Data Revolution (HDR) Institute for Accelerating AI Algorithms for Data Driven Discovery (A3D3) under Cooperative Agreement PHY-2117997. PH is also supported by the Institute for Artificial Intelligence and Fundamental Interactions (IAIFI), under the NSF grant #PHY-2019786. We acknowledge the MicroBooNE Collaboration for making publicly available the data sets [5, 6] employed in this work. These data sets consist of simulated neutrino interactions from the Booster Neutrino Beamline overlaid on top of cosmic data collected with the MicroBooNE detector [8]. This work used resources available through the National Research Platform (NRP) at the University of California, Manuscript submitted to ACM

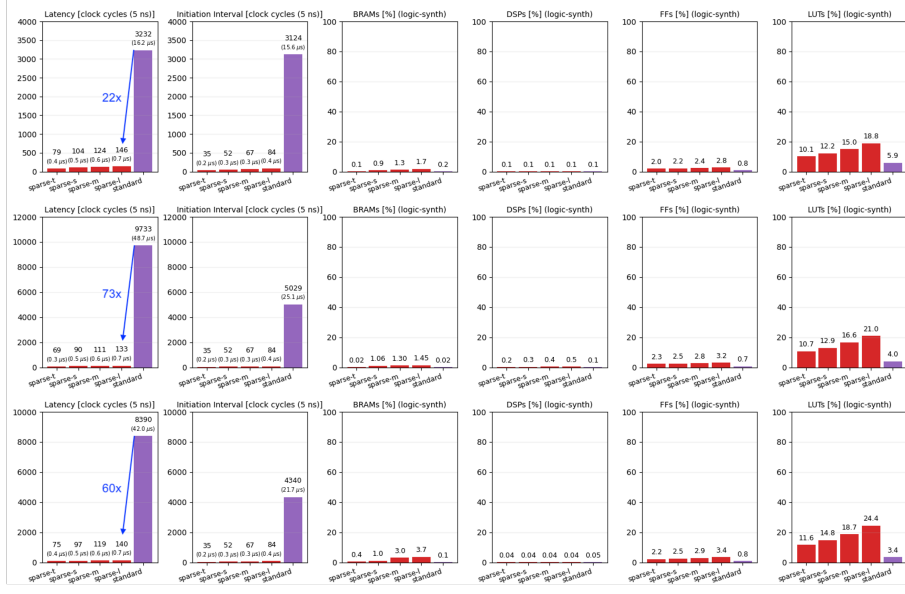


Fig. 16. Synthesis results of standard (purple) and sparse (red) CNNs at 8-bit for MNIST (top), neutrino (middle), and jet tagging (bottom). From left to right: latency, II, BRAMs, DSPs, FFs, and LUTs. Latency and II are measured in clock cycles (cc) with 5 ns clock period. Resource utilization is obtained after the logic synthesis step.

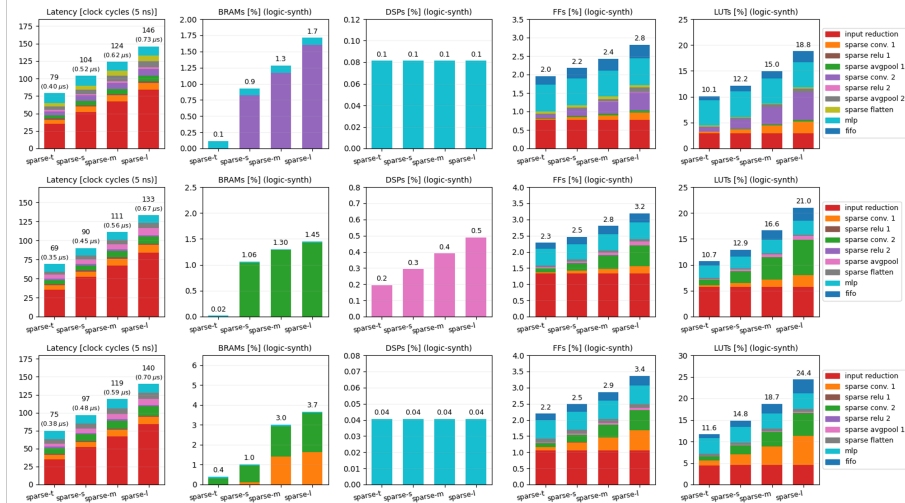


Fig. 17. Per-layer resource breakdown for 8-bit sparse CNNs on MNIST (top), neutrino (middle), and jet tagging (bottom). Latency is measured in clock cycles (cc) with 5 ns clock period. From left to right: latency, BRAMs, DSPs, FFs, and LUTs.

San Diego [57]. NRP has been developed, and is supported in part, by funding from National Science Foundation, from awards 1730158, 1540112, 1541349, 1826967, 2112167, 2100237, and 2120019, as well as additional funding from community partners.

## References

- [1] Georges Aad et al. 2020. Operation of the ATLAS trigger system in Run 2. *JINST* 15, 10 (2020), P10004. arXiv:2007.12539 [physics.ins-det] doi:10.1088/1748-0221/15/10/P10004
- [2] Thea Arrestad et al. 2021. Fast convolutional neural networks on FPGAs with hls4ml. *Mach. Learn. Sci. Tech.* 2, 4 (2021), 045015. arXiv:2101.05108 [cs.LG] doi:10.1088/2632-2153/ac0ea1
- [3] Thea Arrestad et al. 2022. The Dark Machines Anomaly Score Challenge: Benchmark Data and Model Independent Event Classification for the Large Hadron Collider. *SciPost Phys.* 12, 1 (2022), 043. arXiv:2105.14027 [hep-ph] doi:10.21468/SciPostPhys.12.1.043
- [4] B. Abi et al. 2020. Neutrino interaction classification with a convolutional neural network in the DUNE far detector. *Phys. Rev. D* 102, 9 (2020), 092003. arXiv:2006.15052 [physics.ins-det] doi:10.1103/PhysRevD.102.092003
- [5] Polina Abratenko et al. 2022. *MicroBooNE BNB Electron Neutrino Overlay Sample (With Wire Info)*. doi:10.5281/zenodo.7262140
- [6] Polina Abratenko et al. 2022. *MicroBooNE BNB Inclusive Overlay Sample (With Wire Info)*. doi:10.5281/zenodo.7262009
- [7] R. Acciari et al. 2017. Convolutional Neural Networks Applied to Neutrino Events in a Liquid Argon Time Projection Chamber. *JINST* 12, 03 (2017), P03011. arXiv:1611.05531 [physics.ins-det] doi:10.1088/1748-0221/12/03/P03011
- [8] R. Acciari et al. 2017. Design and Construction of the MicroBooNE Detector. *JINST* 12, 02 (2017), P02017. arXiv:1612.05824 [physics.ins-det] doi:10.1088/1748-0221/12/02/P02017
- [9] AMD. 2023. Vitis Libraries (2023.1). [https://docs.amd.com/r/2023.1-English/Vitis\\_Libraries/index.html](https://docs.amd.com/r/2023.1-English/Vitis_Libraries/index.html).
- [10] A. Aurisano, A. Radovic, D. Rocco, A. Himmel, M. D. Messier, E. Niner, G. Pawloski, F. Psihas, A. Sousa, and P. Vahle. 2016. A Convolutional Neural Network Neutrino Event Classifier. *JINST* 11, 09 (2016), P09001. arXiv:1604.01444 [hep-ex] doi:10.1088/1748-0221/11/09/P09001
- [11] Michaela Blott, Thomas B Preußer, Nicholas J Fraser, Giulio Gambardella, Kenneth O'Brien, Yaman Umuroglu, Miriam Leeser, and Kees Vissers. 2018. FINN-R: An end-to-end deep-learning framework for fast exploration of quantized neural networks. *ACM Transactions on Reconfigurable Technology and Systems (TRETS)* 11, 3 (2018), 1–23.
- [12] Anja Butter et al. 2019. The Machine Learning landscape of top taggers. *SciPost Phys.* 7 (2019), 014. arXiv:1902.09914 [hep-ph] doi:10.21468/SciPostPhys.7.1.014
- [13] Matteo Cacciari, Gavin P. Salam, and Gregory Soyez. 2008. The anti- $k_t$  jet clustering algorithm. *JHEP* 04 (2008), 063. arXiv:0802.1189 [hep-ph] doi:10.1088/1126-6708/2008/04/063
- [14] François Chollet et al. 2015. Keras. <https://keras.io>.
- [15] Christopher Choy, JunYoung Gwak, and Silvio Savarese. 2019. 4D Spatio-Temporal ConvNets: Minkowski Convolutional Neural Networks. In *Proceedings of the IEEE Conference on Computer Vision and Pattern Recognition*. 3075–3084.
- [16] Seokju Chung, Jack Cleeve, Akshay Malige, Georgia Karagiorgi, Lino Gerlach, Adrian A. Pol, and Isobel Ojalvo. 2025. Real-time Anomaly Detection for Liquid Argon Time Projection Chambers. (9 2025). arXiv:2509.21817 [hep-ex]
- [17] Andrea Coccato, Francesco Armando Di Bello, Stefano Giagu, Lucrezia Rambelli, and Nicola Stocchetti. 2023. Fast neural network inference on FPGAs for triggering on long-lived particles at colliders. *Mach. Learn. Sci. Tech.* 4, 4 (2023), 045040. arXiv:2307.05152 [hep-ex] doi:10.1088/2632-2153/ad087a
- [18] Claudiomir N. Coelho, Aki Kuusela, Shan Li, Hao Zhuang, Thea Arrestad, Vladimir Loncar, Jennifer Ngadiuba, Maurizio Pierini, Adrian Alan Pol, and Sioni Summers. 2021. Automatic heterogeneous quantization of deep neural networks for low-latency inference on the edge for particle detectors. *Nature Mach. Intell.* 3 (2021), 675–686. arXiv:2006.10159 [physics.ins-det] doi:10.1038/s42256-021-00356-5
- [19] ATLAS Collaboration. 2018. Technical Design Report for the Phase-II Upgrade of the ATLAS TDAQ System. *ATLAS Technical Design Report* CERN-LHCC-2017-020, ATLAS-TDR-029 (2018). doi:10.17181/CERN.2LBB.4IAL
- [20] CMS Collaboration. 2020. The Phase-2 Upgrade of the CMS Level-1 Trigger. *CMS Technical Design Report* CERN-LHCC-2020-004, CMS-TDR-021 (2020).
- [21] CMS Collaboration. 2023. Level-1 Trigger Calorimeter Image Convolutional Anomaly Detection Algorithm. (2023). <https://cds.cern.ch/record/2879816>
- [22] CMS Collaboration. 2024. Model-Independent Real-Time Anomaly Detection at the CMS Level-1 Calorimeter Trigger with CICADA. (2024). <https://cds.cern.ch/record/2917884>
- [23] Luke de Oliveira, Michael Kagan, Lester Mackey, Benjamin Nachman, and Ariel Schwartzman. 2016. Jet-images – deep learning edition. *JHEP* 07 (2016), 069. arXiv:1511.05190 [hep-ph] doi:10.1007/JHEP07(2016)069
- [24] Laura Dominé and Kazuhiro Terao. 2020. Scalable deep convolutional neural networks for sparse, locally dense liquid argon time projection chamber data. *Phys. Rev. D* 102, 1 (2020), 012005. arXiv:1903.05663 [hep-ex] doi:10.1103/PhysRevD.102.012005
- [25] Javier Duarte et al. 2018. Fast inference of deep neural networks in FPGAs for particle physics. *JINST* 13, 07 (2018), P07027. arXiv:1804.06913 [physics.ins-det] doi:10.1088/1748-0221/13/07/P07027
- [26] FastML Team. 2025. *fastmachinelearning/hls4ml*. doi:10.5281/zenodo.1201549
- [27] Simone Francescato et al. 2021. Model compression and simplification pipelines for fast deep neural network inference in FPGAs in HEP. *Eur. Phys. J. C* 81, 11 (2021), 969. doi:10.1140/epjc/s10052-021-09770-w [Erratum: Eur.Phys.J.C 81, 1064 (2021)].
- [28] Abhijith Gandrakota. 2025. Realtime Anomaly Detection at the L1 Trigger of CMS Experiment. *PoS ICHEP2024* (2025), 1025. arXiv:2411.19506 [hep-ex] doi:10.22323/1.476.1025
- [29] Nicolò Ghielmetti et al. 2022. Real-time semantic segmentation on FPGAs for autonomous vehicles with hls4ml. *Mach. Learn. Sci. Tech.* (2022). arXiv:2205.07690 [cs.CV] doi:10.1088/2632-2153/ac9cb5

[30] Ekaterina Govorkova et al. 2022. Autoencoders on field-programmable gate arrays for real-time, unsupervised new physics detection at 40 MHz at the Large Hadron Collider. *Nature Mach. Intell.* 4 (2022), 154–161. arXiv:2108.03986 [physics.ins-det] doi:10.1038/s42256-022-00441-3

[31] Ben Graham. 2015. Sparse 3D convolutional neural networks. arXiv:1505.02890 [cs.CV] <https://arxiv.org/abs/1505.02890>

[32] Benjamin Graham, Martin Engelcke, and Laurens van der Maaten. 2018. 3D Semantic Segmentation with Submanifold Sparse Convolutional Networks. In *2018 IEEE/CVF Conference on Computer Vision and Pattern Recognition (CVPR)*. 9224–9232. arXiv:1711.10275 doi:10.1109/CVPR.2018.00961

[33] Zhixing Jiang, Dennis Yin, Yihui Chen, Elham E. Khoda, Scott Hauck, Shih-Chieh Hsu, Ekaterina Govorkova, Philip Harris, Vladimir Loncar, and Eric A. Moreno. 2025. Low latency transformer inference on FPGAs for physics applications with hls4ml. *JINST* 20, 04 (2025), P04014. arXiv:2409.05207 [cs.LG] doi:10.1088/1748-0221/20/04/P04014

[34] Gregor Kasieczka et al. 2021. The LHC Olympics 2020 a community challenge for anomaly detection in high energy physics. *Rept. Prog. Phys.* 84, 12 (2021), 124201. arXiv:2101.08320 [hep-ph] doi:10.1088/1361-6633/ac36b9

[35] Gregor Kasieczka, Tilman Plehn, Michael Russell, and Torben Schell. 2017. Deep-learning Top Taggers or The End of QCD? *JHEP* 05 (2017), 006. arXiv:1701.08784 [hep-ph] doi:10.1007/JHEP05(2017)006

[36] Elham E. Khoda et al. 2023. Ultra-low latency recurrent neural network inference on FPGAs for physics applications with hls4ml. *Mach. Learn. Sci. Tech.* 4, 2 (2023), 025004. arXiv:2207.00559 [cs.LG] doi:10.1088/2632-2153/acc0d7

[37] Diederik P. Kingma and Jimmy Ba. 2017. Adam: A Method for Stochastic Optimization. arXiv:1412.6980 [cs.LG]

[38] Yann LeCun, Yoshua Bengio, and Geoffrey Hinton. 2015. Deep learning. *Nature* 521 (2015), 436–444. doi:10.1038/nature14539

[39] Yann LeCun and Corinna Cortes. 2010. MNIST handwritten digit database. <http://yann.lecun.com/exdb/mnist/>

[40] Baoyuan Liu, Min Wang, Hassan Foroosh, Marshall Tappen, and Marianna Pensky. 2015. Sparse Convolutional Neural Networks. In *2015 IEEE Conference on Computer Vision and Pattern Recognition (CVPR)*. 806–814. doi:10.1109/CVPR.2015.7298681

[41] Liqiang Lu, Jiaming Xie, Ruirui Huang, Jiansong Zhang, Wei Lin, and Yun Liang. 2019. An Efficient Hardware Accelerator for Sparse Convolutional Neural Networks on FPGAs. In *2019 IEEE 27th Annual International Symposium on Field-Programmable Custom Computing Machines (FCCM)*. 17–25. doi:10.1109/FCCM.2019.00013

[42] Leandro Maglianella, Lorenzo Nicoletti, Stefano Giagu, Christian Napoli, and Simone Scardapane. 2023. Convergent Approaches to AI Explainability for HEP Muonic Particles Pattern Recognition. *Comput. Softw. Big Sci.* 7, 1 (2023), 8. doi:10.1007/s41781-023-00102-z

[43] Eric A. Moreno, Olmo Cerri, Javier M. Duarte, Harvey B. Newman, Thong Q. Nguyen, Avikar Periwal, Maurizio Pierini, Aidana Serikova, Maria Spiropulu, and Jean-Roch Vlimant. 2020. JEDI-net: a jet identification algorithm based on interaction networks. *Eur. Phys. J. C* 80, 1 (2020), 58. arXiv:1908.05318 [hep-ex] doi:10.1140/epjc/s10052-020-7608-z

[44] Adam Paszke, Sam Gross, Francisco Massa, Gal Lerer, James Bradbury, Gregory Chanan, Trevor Killeen, Zeming Lin, Naresh Gimelshein, Luca Antiga, et al. 2019. PyTorch: An Imperative Style, High-Performance Deep Learning Library. *Advances in Neural Information Processing Systems* 32 (2019).

[45] Maurizio Pierini, Javier Mauricio Duarte, Nhan Tran, and Marat Freytsis. 2020. *HLS4ML LHC Jet dataset (150 particles)*. doi:10.5281/zenodo.3602260

[46] Adrian Alan Pol et al. 2021. Jet Single Shot Detection. *EPJ Web Conf.* 251 (2021), 04027. arXiv:2105.05785 [hep-ex] doi:10.1051/epjconf/202125104027

[47] Albert M Sirunyan et al. 2020. Performance of the CMS Level-1 trigger in proton-proton collisions at  $\sqrt{s} = 13$  TeV. *JINST* 15, 10 (2020), P10017. arXiv:2006.10165 [hep-ex] doi:10.1088/1748-0221/15/10/P10017

[48] Sioni Summers et al. 2020. Fast inference of Boosted Decision Trees in FPGAs for particle physics. *JINST* 15, 05 (2020), P05026. arXiv:2002.02534 [physics.comp-ph] doi:10.1088/1748-0221/15/05/P05026

[49] Chang Sun, Thea K. Arrestad, Vladimir Loncar, Jennifer Ngadiuba, and Maria Spiropulu. 2024. Gradient-based Automatic Mixed Precision Quantization for Neural Networks On-Chip. (5 2024). arXiv:2405.00645 [cs.LG] doi:10.7907/hq8jd-rhg30

[50] Haotian Tang, Zhijian Liu, Xiuyu Li, Yujun Lin, and Song Han. 2022. TorchSparse: Efficient Point Cloud Inference Engine. In *Conference on Machine Learning and Systems (MLSys)*.

[51] Haotian Tang, Shang Yang, Zhijian Liu, Ke Hong, Zhongming Yu, Xiuyu Li, Guohao Dai, Yu Wang, and Song Han. 2023. TorchSparse++: Efficient Training and Inference Framework for Sparse Convolution on GPUs. In *IEEE/ACM International Symposium on Microarchitecture (MICRO)*.

[52] Naif Tarafdar, Giuseppe Di Guglielmo, Philip C. Harris, Jeffrey D. Krupa, Vladimir Loncar, Dylan S. Rankin, Nhan Tran, Zhenbin Wu, Qianfeng Clark Shen, and Paul Chow. 2022. Algean: An Open Framework for Deploying Machine Learning on Heterogeneous Clusters. *ACM Trans. Reconf. Tech. Syst.* 15, 3 (2022), 1–32. doi:10.1145/3482854

[53] Ho Fung Tsoi, Vladimir Loncar, Sridhara Dasu, and Philip Harris. 2025. SymbolNet: neural symbolic regression with adaptive dynamic pruning for compression. *Mach. Learn. Sci. Tech.* 6, 1 (2025), 015021. arXiv:2401.09949 [cs.LG] doi:10.1088/2632-2153/adaad8

[54] Ho Fung Tsoi, Adrian Alan Pol, Vladimir Loncar, Ekaterina Govorkova, Miles Cranmer, Sridhara Dasu, Peter Elmer, Philip Harris, Isobel Ojalvo, and Maurizio Pierini. 2024. Symbolic Regression on FPGAs for Fast Machine Learning Inference. *EPJ Web Conf.* 295 (2024), 09036. arXiv:2305.04099 [cs.LG] doi:10.1051/epjconf/202429509036

[55] Yaman Umuroglu, Nicholas J. Fraser, Giulio Gambardella, Michaela Blott, Philip Leong, Magnus Jahre, and Kees Vissers. 2017. FINN: A Framework for Fast, Scalable Binarized Neural Network Inference. In *Proceedings of the 2017 ACM/SIGDA International Symposium on Field-Programmable Gate Arrays (FPGA '17)*. ACM, 65–74.

[56] Jure Vreča and Anton Biasizzo. 2025. Generating Direct Logic Circuit Implementations of Deeply Quantized Neural Networks Using Chisel4ml. *Electronics* 14, 5 (2025). doi:10.3390/electronics14050849

- [57] Derek Weitzel, Ashton Graves, Sam Albin, Huijun Zhu, Frank Wuerthwein, Mahidhar Tatineni, Dmitry Mishin, Elham Khoda, Mohammad Sada, Larry Smarr, Thomas DeFanti, and John Graham. 2025. The National Research Platform: Stretched, Multi-Tenant, Scientific Kubernetes Cluster. In *Practice and Experience in Advanced Research Computing 2025: The Power of Collaboration (PEARC '25)*. Article 69, 5 pages. [doi:10.1145/3708035.3736060](https://doi.org/10.1145/3708035.3736060)
- [58] Xilinx. 2020. Vivado Design Suite User Guide: High-Level Synthesis. [https://www.xilinx.com/support/documentation/sw\\_manuals/xilinx2020\\_1/ug902-vivado-high-level-synthesis.pdf](https://www.xilinx.com/support/documentation/sw_manuals/xilinx2020_1/ug902-vivado-high-level-synthesis.pdf).
- [59] Yan Yan, Yuxing Mao, and Bo Li. 2018. SECOND: Sparsely Embedded Convolutional Detection. *Sensors* 18, 10 (2018). [doi:10.3390/s18103337](https://doi.org/10.3390/s18103337)
- [60] Chaoyang Zhu, Kejie Huang, Shuyuan Yang, Ziqi Zhu, Hejia Zhang, and Haibin Shen. 2020. An Efficient Hardware Accelerator for Structured Sparse Convolutional Neural Networks on FPGAs. *IEEE Trans. Very Large Scale Integr. Syst.* 28, 9 (Sept. 2020), 1953–1965. [doi:10.1109/TVLSI.2020.3002779](https://doi.org/10.1109/TVLSI.2020.3002779)
- [61] I. Zurbano Fernandez et al. 2020. High-Luminosity Large Hadron Collider (HL-LHC): Technical design report. 10/2020 (12 2020). [doi:10.23731/CYRM-2020-0010](https://doi.org/10.23731/CYRM-2020-0010)

**Algorithm 3:** Sparse Activation in HLS

---

```

Inputs :sparse feature array  $a_{\text{feat}}^{\text{in}}[0..N_{\text{active}}^{\text{max}} \cdot C - 1]$ 
Outputs :sparse feature array  $a_{\text{feat}}^{\text{out}}[0..N_{\text{active}}^{\text{max}} \cdot C - 1]$ 
1 Procedure SparseActivation // element-wise activation on sparse features:
2   for  $i \leftarrow 0$  to  $N_{\text{active}}^{\text{max}} \cdot C - 1$  do
3      $a_{\text{feat}}^{\text{out}}[i] \leftarrow \text{Act}(a_{\text{feat}}^{\text{in}}[i])$ 

```

---

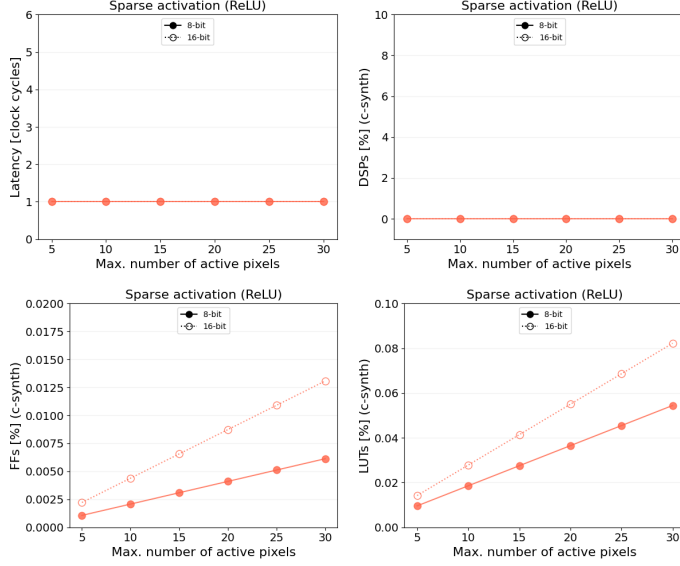


Fig. 18. Scalings of the sparse activation layer on an FPGA for different  $N_{\text{active}}^{\text{max}}$ : latency (upper left), DSPs (upper right), FFs (lower left), and LUTs (lower right). Resource utilization is obtained from the HLS C-synthesis step.

## A appendix

### A.1 Sparse activation in HLS and scaling

The algorithmic details are given in Alg. 3. For scaling, we use ReLU and scan  $N_{\text{active}}^{\text{max}}$  from 5 to 30 in steps of 5. Fig. 18 reports latency and resource utilization. The activation loop is fully unrolled, so the layer finishes in one clock cycle and uses no DSPs. FF/LUT usage increases with  $N_{\text{active}}^{\text{max}}$  because more elements are processed in parallel.

### A.2 Sparse pooling in HLS and scaling

The algorithmic details are given in Alg. 4. For scaling, we use average-pooling as an example, test  $C_{\text{in}} \in \{1, 2, 3\}$ , and scan  $N_{\text{active}}^{\text{max}}$  from 5 to 30 in steps of 5. Fig. 19 shows latency and resource utilization. The latency curves across  $C_{\text{in}}$  coincide because the channel loop is unrolled. No DSPs are used; FF/LUT usage increases with  $N_{\text{active}}^{\text{max}}$  and  $C_{\text{in}}$  due to more parallel comparisons and accumulators.

### A.3 Sparse flatten in HLS and scaling

The algorithmic details are given in Alg. 5. For scaling, we test flat output sizes  $C_{\text{out}} \in \{40, 60, 80, 100\}$  and scan  $N_{\text{active}}^{\text{max}}$  from 5 to 30 in steps of 5. Fig. 20 shows latency and resource utilization. The latency is essentially independent of the

**Algorithm 4:** Sparse Pooling (Avg) in HLS

---

**Inputs** :sparse feature array  $a_{\text{feat}}^{\text{in}}[0..N_{\text{active}}^{\text{max}} \cdot C - 1]$ , sparse hash array  $a_{\text{hash}}^{\text{in}}[0..N_{\text{active}}^{\text{max}} \cdot 2 - 1]$ , pool size  $P$   
**Outputs**:sparse feature array  $a_{\text{feat}}^{\text{out}}[0..N_{\text{active}}^{\text{max}} \cdot C - 1]$ , sparse hash array  $a_{\text{hash}}^{\text{out}}[0..N_{\text{active}}^{\text{max}} \cdot 2 - 1]$

---

**1 Procedure** *SparseAvgPool*:

```

1  // compute pooled coords and fill output hash
2  for  $i \leftarrow 0$  to  $N_{\text{active}}^{\text{max}} - 1$  do
3       $a_{\text{hash}}^{\text{out}}[2i] \leftarrow \lfloor (a_{\text{hash}}^{\text{in}}[2i] - 1)/P \rfloor + 1$ 
4       $a_{\text{hash}}^{\text{out}}[2i + 1] \leftarrow \lfloor (a_{\text{hash}}^{\text{in}}[2i + 1] - 1)/P \rfloor + 1$ 
5  // loop over output hash
6  for  $i \leftarrow 0$  to  $N_{\text{active}}^{\text{max}} - 1$  do
7      // loop over channels
8      for  $c \leftarrow 0$  to  $C - 1$  do
9           $A \leftarrow 0$ 
10         // collect pixels that map to same pool
11         for  $j \leftarrow 0$  to  $N_{\text{active}}^{\text{max}} - 1$  do
12             if  $a_{\text{hash}}^{\text{out}}[2j] = a_{\text{hash}}^{\text{out}}[2i] \text{ and } a_{\text{hash}}^{\text{out}}[2j + 1] = a_{\text{hash}}^{\text{out}}[2i + 1]$  then
13                  $A \leftarrow A + a_{\text{feat}}^{\text{in}}[C \cdot j + c]$ 
14              $a_{\text{feat}}^{\text{in}}[C \cdot j + c] \leftarrow 0$  // after consume, mask to avoid double counting
15          $a_{\text{feat}}^{\text{out}}[C \cdot i + c] \leftarrow A/P$ 

```

---

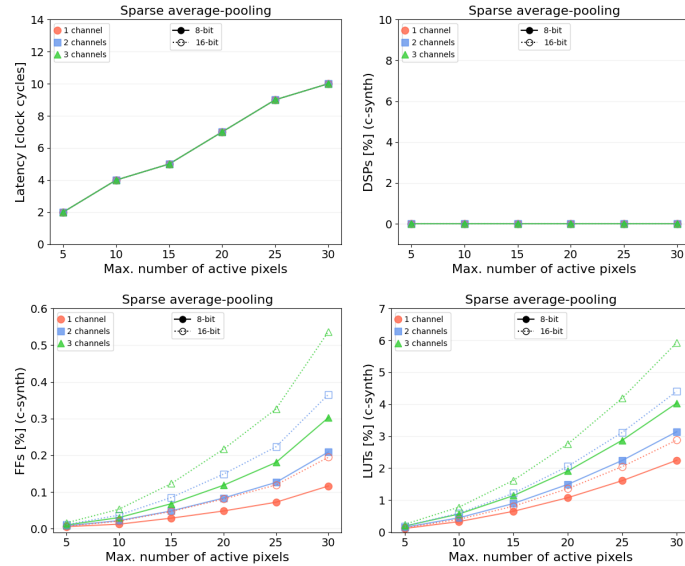


Fig. 19. Scalings of the sparse pooling layer on an FPGA for different number of channels and  $N_{\text{active}}^{\text{max}}$ : latency (upper left), DSPs (upper right), FFs (lower left), and LUTs (lower right). Resource utilization is obtained from the HLS C-synthesis step.

small flat output size because *HWC* initialization is fully unrolled. Because this is address generation plus writes, DSP usage is 0, while FF/LUT usage increases with  $N_{\text{active}}^{\text{max}}$  and  $C_{\text{out}}$ .

**Algorithm 5:** Sparse Flatten in HLS

---

**Inputs** :sparse feature array  $a_{\text{feat}}^{\text{in}}[0..N_{\text{active}}^{\text{max}} \cdot C - 1]$ , sparse hash array  $a_{\text{hash}}^{\text{in}}[0..N_{\text{active}}^{\text{max}} \cdot 2 - 1]$ , dim  $(H, W, C)$   
**Outputs**:flat dense array  $X[0..HWC - 1]$

**Procedure** *SparseFlatten* // scatter sparse pixels into flat dense array (channel-last):

- 1 **for**  $j \leftarrow 0$  **to**  $HWC - 1$  **do**  
  - 2    $X[j] \leftarrow 0$  // zero-initialize
  - 3   **for**  $i \leftarrow 0$  **to**  $N_{\text{active}}^{\text{max}} - 1$  **do**  
    - 4      $\text{pix} \leftarrow (a_{\text{hash}}^{\text{in}}[2i] - 1) \cdot W + (a_{\text{hash}}^{\text{in}}[2i + 1] - 1)$
    - 5     **for**  $c \leftarrow 0$  **to**  $C - 1$  **do**  
      - 6        $X[C \cdot \text{pix} + c] \leftarrow a_{\text{feat}}^{\text{in}}[C \cdot i + c]$  // scatter

---

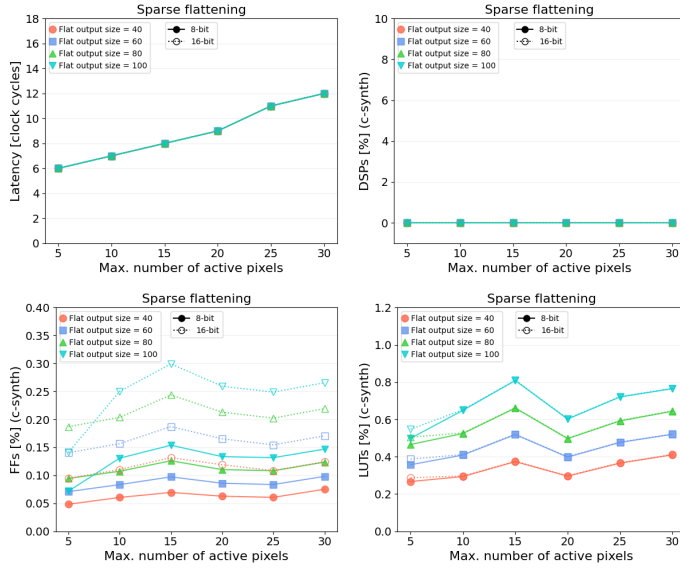


Fig. 20. Scalings of the sparse flattening layer on an FPGA for different flat output array size and  $N_{\text{active}}^{\text{max}}$ : latency (upper left), DSPs (upper right), FFs (lower left), and LUTs (lower right). Resource utilization is obtained from the HLS C-synthesis step.

#### A.4 Synthesis results for 16-bit models

Fig. 21 and Fig. 22 summarize results of the 16-bit models. Latencies are similar to the 8-bit models because of same loop structures in architectural design. DSP usage increases primarily because arithmetic such as multiplications are preferably mapped to DSPs at higher bit-width by Vivado.

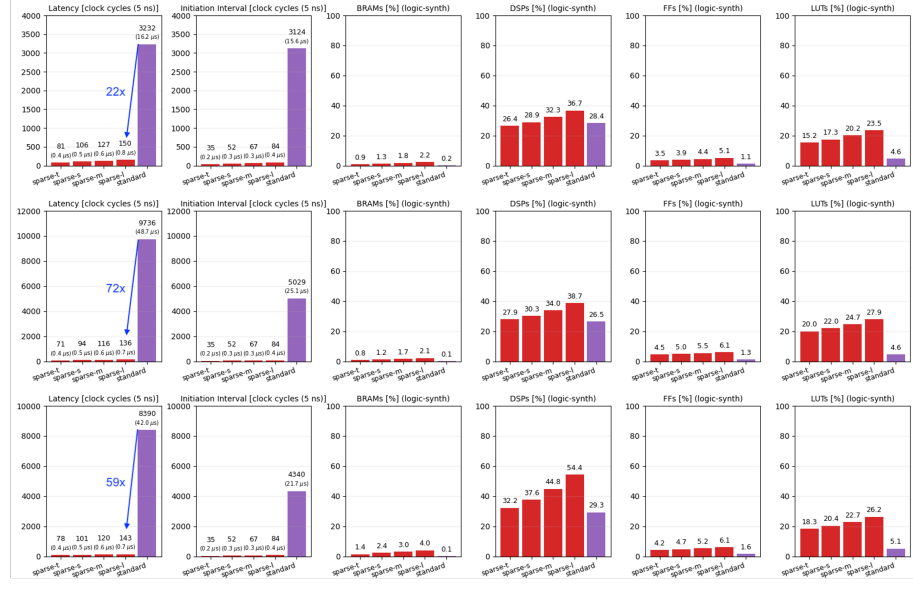


Fig. 21. Synthesis results of standard (purple) and sparse (red) CNNs at 16-bit for MNIST (top), neutrino (middle), and jet tagging (bottom). From left to right: latency, II, BRAMs, DSPs, FFs, and LUTs. Latency and II are measured in clock cycles (cc) with 5 ns clock period. Resource utilization is obtained after the logic synthesis step.

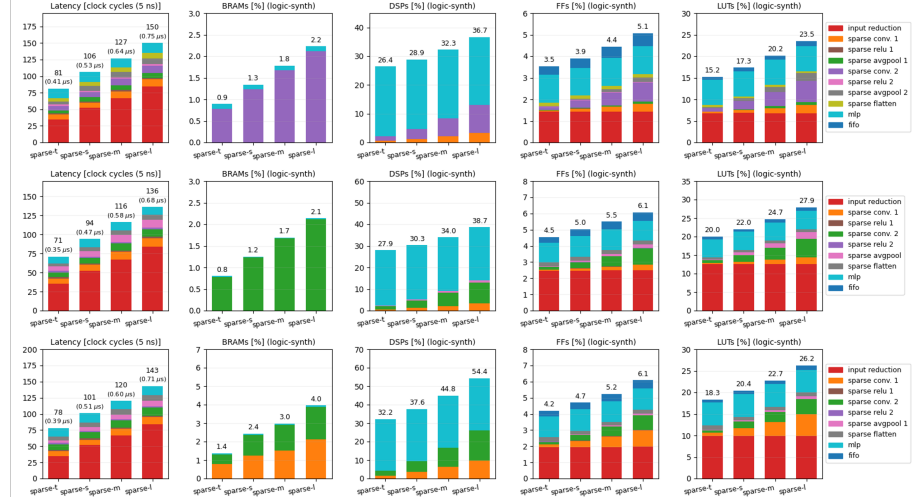


Fig. 22. Per-layer resource breakdown for 16-bit sparse CNNs on MNIST (top), neutrino (middle), and jet tagging (bottom). Latency is measured in clock cycles (cc) with 5 ns clock period. From left to right: latency, BRAMs, DSPs, FFs, and LUTs.